Investigating the link between mineral dust hematite content and intensive optical properties by means of lidar measurements and aerosol modelling

Sofía Gómez Maqueo Anaya[1], Dietrich Althausen[1], Julian Hofer[1], Moritz Haarig[1], Ulla Wandinger[1], Bernd Heinold[1], Ina Tegen[1], Matthias Faust[1], Holger Baars[1], Albert Ansmann[1], Ronny Engelmann[1], Annett Skupin[1], Birgit Heese[1], and Kerstin Schepanski[2]

[1]Leibniz Institute for Tropospheric Research (TROPOS), Leipzig, Germany
[2]Free University of Berlin, Berlin, Germany

Correspondence: Sofía Gómez Maqueo Anaya (maqueo@tropos.de)

Abstract. This study investigates the relationship between lidar-measured intensive optical properties of Saharan dust and simulated hematite content, using data collected during the Joint Aeolus Tropical Atlantic Campaign (JATAC) in 2021 and 2022. Measurements were taken in Mindelo, São Vicente, Cabo Verde. The study aims to determine how variations in hematite content influence the intensive optical properties of dust particles, particularly in the ultraviolet-visible (UV-VIS) spectrum.
5 Given the well-documented impact of hematite on the extinction properties of dust, especially absorption in the UV-VIS range, our hypothesis is that these effects will be detectable in lidar measurements. Specifically, this study focuses on the lidar ratio, particle depolarization ratio and backscatter- and extinction-related Ångström exponents at 355 nm and 532 nm wavelengths. By analyzing dust plume cases separately regarding their size differences, the strongest positive correlation was identified between the backscatter-related Ångström exponent and hematite fraction (rR^2 = ~~0.87, p=0.02~~0.63). These findings contribute
10 to improving the representation of dust in atmospheric models and refining calculations of its direct radiative effect, which often overlook the variability in mineralogical composition in their dust descriptions.

1 Introduction

Mineral dust aerosols are present all around the world. They contribute significantly to the global and regional aerosol loading (Weinzierl et al., 2017), and correspond to a big part of the atmospheric aerosol burden by mass (Kok et al., 2017). Specifically,
15 the Sahara Desert and the Sahel contributes around 50% of the global dust emissions and mass loading (Kok et al., 2021). During transport, dust interacts with the atmosphere in a variety of ways. It modifies the energy balance of Earth through multiple mechanisms, each producing a radiative effect. These impacts can be instantaneous, such as dust scattering and absorption radiation, or may take time to adjust, such as dust altering cloud covers (Boucher et al., 2013). The immediate radiation interactions are well studied; it is known that dust absorbs and scatters solar shortwave and terrestrial longwave
20 radiation depending on its composition (Kok et al., 2017). These interactions have the potential to modify the atmospheric radiation balance from meso- to macro-scale (Kok et al., 2023; Mahowald et al., 2010; Li et al., 2024). However, the magnitude

and sign of this dust radiative effect is still uncertain (Highwood and Ryder, 2014; Kok et al., 2017), one of the major sources of this uncertainty is insufficient knowledge regarding dust absorption properties (Balkanski et al., 2007; Di Biagio et al., 2020; Go et al., 2022). Since dust aerosols are a complex assemblage of various minerals with their distinct physicochemical

25 properties (Formenti et al., 2011), differences in their atmospheric radiative impact will arise as a consequence of distinct mineralogical content.

In order to predict and model the direct radiative effect of mineral dust, vertical profiles of its optical properties are part of the basic necessary input. Among these, the profile of the extinction-to-backscatter ratio, known as the lidar ratio (S), is particularly critical (Veselovskii et al., 2020). The lidar ratio, being an intensive optical property (independent of aerosol

30 quantity), is commonly used to characterize mineral dust. However, it has a complex dependency ~~to~~ on three major parameters: size, shape and composition (Wandinger et al., 2023). Several studies have aligned differences in dust optical properties to distinct mineralogical content according to source regions (Di Biagio et al., 2017, 2019; Lafon et al., 2004; Sokolik and Toon, 1999; Wagner et al., 2012). Some studies have specifically linked the changes ~~in the~~ of S to different source regions (Esselborn et al., 2009) and even further to the changes that these differences cause on the dust complex refractive index (CRI) (Go

35 et al., 2022; Schuster et al., 2012; Veselovskii et al., 2020). Specifically, when iron oxides are present in dust particles, the imaginary part of the CRI changes across the radiation spectrum, with an increase in the UV-VIS range. Consequently, they are considered as effective absorbers of the shortwave radiation (Di Biagio et al., 2019; Moosmüller et al., 2012; Sokolik et al., 1993; Sokolik and Toon, 1996; Wagner et al., 2012; Zhang et al., 2024). ~~However,~~ Moreover, variations of the imaginary part of the CRI are linked to changes of backscattering properties of aerosols in the UV-VIS part of the spectra, even for

40 minor variations on the order of 10^{-3} (De Leeuw and Lamberts, 1987; Miffre et al., 2020). These variations are consistent with the changes in the imaginary part of the CRI observed by Di Biagio et al. (2019), which have shown to influence the single-scattering albedo (SSA) of dust. Specifically, at a wavelength of 370 nm, an increase of the imaginary part from 0.0016 to 0.0048 results in a decrease in SSA from 0.95 to 0.75. These changes are further linked to variations in the hematite fraction of 0.5% (Di Biagio et al., 2019).

45 Nonetheless, most characterizations of dust based on lidar measured optical properties treat it as homogeneous, giving way to unique wavelength dependent lidar ratio values that indicate Saharan "pure dust". (Haarig et al., 2017, 2022; Groß et al., 2011, 2015; Müller et al., 2013; Schuster et al., 2012; Tesche et al., 2009a, 2011). These studies specifically suggests that the ~~lidar ratio of dust shows~~ intensive optical properties of dust show no clear regional spectral dependency, despite observed regional spectral variations have been linked to changes in the ~~CRI~~ CR, specially for the lidar ratio and the backscatter-related

50 Ångström exponent (Schuster et al., 2012; Veselovskii et al., 2020). ~~Furthermore, a~~ The sensitivity study by Veselovskii et al. (2020) demonstrates the impact of changes ~~in~~ of the imaginary part of the CRI, due to ~~differences in iron oxide~~ different iron oxide contents in Saharan dust, on the backscatter-related Ångström exponent ~~in~~ for the UV-VIS wavelengths. This relationship is further explored in the laboratory studies by Miffre et al. (2020, 2023), which included particle shape and ~~reveal~~ revealed the non-linearity of the three key physical parameters, size, shape, and composition, affecting the intensive optical

55 properties of dust. Specifically they measured significant impacts of the variations in the complex refractive index for both the backscatter-related Ångström exponents and the particle depolarization ratio for the UV-VIS wavelength range.

However, several limitations must be considered. Miffre et al. (2020, 2023) conducted their studies in a laboratory setting, which findings may not directly translate to atmospheric conditions, as other atmospheric constituents can have an impact on the measurements. In Veselovskii et al. (2020)'s study, measurements were taken near to an active dust-emitting area, making the presence of larger particles highly likely. ~~Since the lidar ratio is~~ For the intensive optical properties where an impact of the complex refractive index has been documented, both, the backscatter-related Ångström exponents and the lidar ratio are particularly sensitive to changes in particle size~~as~~. Which impact are illustrated by Fig. 1 in Miffre et al. (2020) backscatter-related Ångström exponents and by the Fig. 5 in Wandinger et al. (2023) and Fig. 15 in Zhang et al. (2024) ~~, both particle size~~ for the lidar ratio. Particle size, shape, and composition influence the measurements, making it challenging to isolate the effects of each factor. Additionally, the ~~measurements were conducted~~ lidar measurements conducted by Veselovskii et al. (2020) were taken during a season well known for increased biomass burning activity, leading to frequent encounters with polluted dust in the atmosphere. This pollution alters the measured optical properties, particularly in the UV-VIS spectrum (Heinold et al., 2011; Müller et al., 2009; Tesche et al., 2011), adding another layer of complexity in disentangling compositional effects on ~~the~~ both the backscatter-related Ångström exponents and the lidar ratio.

The transport of mineral dust from the Sahara Desert towards the Atlantic Ocean is well-documented (Schepanski et al., 2009, 2017; Tegen et al., 2013; Wagner et al., 2016). During the northern hemispheric (NH) winter months, polluted dust is observed at near-surface layers, complicating the distinction between dust and other aerosols, such as biomass burning aerosols, in lidar measurements. In contrast, during NH summer months, dust is elevated in the atmosphere (Schepanski et al., 2009). Dust transport for the NH summer months is above the marine boundary layer, i.e., on the free troposphere which in turn means that dust transport from the Sahara Desert towards the Atlantic Ocean is more direct. Lidar measurements taken during this time show that the elevated dust layers typically contain lower levels of pollution from other aerosols (Esselborn et al., 2009; Freudenthaler et al., 2009; Haarig et al., 2017, 2019; Groß et al., 2015; Tesche et al., 2009b). Therefore, this study focuses on lidar-measured cases from a remote site in Cabo Verde, to avoid interference from freshly emitted large dust particles, along the mineral dust transport pathway from the Sahara Desert to the Atlantic Ocean. ~~The~~ These lidar measurements were taken in Mindelo, São Vicente, Cabo Verde (16°52'39.9"N, 24°59'42.3"W) during NH summer months, from June to September of 2021 and 2022, as part of the Joint Aelous Tropical Atlantic Campaign(s) (JATAC).

~~In this study ,~~ This study investigates the potential to identify dust mineralogy within lidar measured optical properties. By analyzing years of continuous, 24/7 lidar measurements of multiple vertical dust profiles above the marine boundary layer, we aim to ~~explore the relationship between the lidar-measured dust particle's~~ correlate lidar derived intensive optical properties ~~and the modelled~~ of dust particles with modeled iron oxide content ~~obtained~~ from an atmospheric model. Given that previous studies demonstrated the ~~impact~~ ability of iron oxides on ~~the extinction (absorption plus scattering)~~ modifying the imaginary part of the CRI, and the impact of that variation on dust intensive optical properties, particularly ~~in~~ for the UV-VIS specturm ~~,~~ ~~this project~~ (Di Biagio et al., 2019; Miffre et al., 2020, 2023), this work hypothesizes that this effect will manifest in the lidar measured intensive optical properties at 355 nm and 532 nm wavelengths. The aim is to investigate how the iron oxide content, which varies significantly across the Sahara Desert (Formenti et al., 2011, 2014; Scheuvens et al., 2013), affects dust's intensive optical properties. While mineralogical variations within the Sahara Desert are well-known~~and could influence dust optical~~

~~properties~~, just a few atmospheric models account for mineralogy in their mineral dust descriptions (Chatziparaschos et al., 2023; Gonçalves Ageitos et al., 2023; Li et al., 2021; Menut et al., 2020; Pérez García-Pando et al., 2016; Perlwitz et al., 2015a, b; Solomos et al., 2023).

95   On a previous study, Gómez Maqueo Anaya et al. (2024) introduced the global, GMINER (Nickovic et al., 2012), mineralogical dataset into the emission code of the aerosol-atmosphere model COSMO-MUSCAT. The configuration presented in that study is what will be used here. GMINER provides spatial distribution of minerals, including iron oxides minerals, based on the methodology of Claquin et al. (1999). This considers an approximate relation of soil mineral fractions to different soil types by taking into account the size distribution, the chemistry and the color of the soil according to the FAO74 classi-
100   fication (FAO-UNESCO, 1974). However, this approach incurs in a handful of misrepresentations when compared to in-situ measurements (Li et al., 2024; Gonçalves Ageitos et al., 2023). Despite the limitations, Gonçalves Ageitos et al. (2023) found that GMINER dataset fairly reproduces ~~iron oxide~~ the hematite mass content for the Sahara Desert region (see Fig.11(a) from Gonçalves Ageitos et al., 2023). In GMINER, iron oxide minerals are grouped under the name hematite, and so, we will use hematite and iron oxide interchangeably in this paper. Even though, it is noteworthy that the goethite mineral also contains iron
105   oxide and interacts differently with radiation (Di Biagio et al., 2019; Formenti et al., 2014; Go et al., 2022; Wagner et al., 2012), and iron oxides may not always appear as externally mixed aerosols as assumed here (Lafon et al., 2004; Kandler et al., 2009). This study combines the ~~modelled~~ modeled hematite content with the lidar retrieved intensive optical properties to investigate potential correlations between them.

    This paper has the following structure: The methodology begins with a general description of the COSMO-MUSCAT model
110   (Sect. 2.1), followed by a general overview of the lidar system, Polly^{XT} (Sect. 2.2). This is succeeded by an explanation of the data selection (Sect. 2.3) and a description of the comparisons between lidar and model dust layers (Sect. 2.4). The section concludes with a brief outline of the POLIPHON method, which converts lidar measurements into dust mass concentrations (Sect. 2.5). In the results section, a case example is shown in Sect. 3.1 where the vertically resolved optical properties are shown in Sect. 3.1.1 followed by a comparison of the POLIPHON and COSMO-MUSCAT results in Sect. 3.1.2. All case studies are
115   then presented and discussed in Sect. 3.2, the intensive optical properties dependency with hematite is further explored in Sect. 3.2.1 and a separate analysis of the cases due to their size differences is shown in Sect. 3.2.2. Finally, Sect. 4 provides a summary of the ~~project~~ paper and findings and discusses implications for future work.

2 Methodology

2.1 COSMO-MUSCAT

120   COSMO-MUSCAT is a mesoscale atmospheric model system integrated by two online coupled models. COSMO, developed by the German Weather Service (DWD) is a regional forecast model (Baldauf et al., 2011), while MUSCAT is a chemistry transport model that calculates the atmospheric advective transport of aerosols driven by the forecast model (Heinold et al., 2016; Wolke et al., 2012). The meteorological data are updated every 3 hours and the model runs are reinitialized in overlapping cycles every 48 hours. The use of COSMO-MUSCAT regarding the simulation of mineral dust for the Sahara Desert region

125 was been thoroughly validated (Gómez Maqueo Anaya et al., 2024; Heinold et al., 2011; Schepanski et al., 2009, 2016, 2017; Tegen et al., 2013). COSMO-MUSCAT is setup for simulating only the transport of Saharan mineral dust including mineralogy within a domain constrained by the following coordinates: 30.75°W, 38.49°N – 39.32°E, 0.38°S. The horizontal grid spacing is 0.25° (28 km) and the vertical resolution contains 40 levels, with a layer thickness of 20 m above sea level for the first (bottom) layer. The thickness of the subsequent vertical layers varies according to pressure levels, varying from 200 m thickness at 1 km

130 height to 600 m thickness at 4 km height . and a maximum altitude of 21.75 km. The output variables are given for every hour inside of the simulation time. These temporal and spatial resolutions imply a very big difference when compared to a fixed lidar point measurement which is able to retrieve aerosol signals with a significantly higher vertical and temporal resolutions. The difference of these resolutions has to be taken into account when analyzing the results, specially considering that the model gives average dust mass concentration values for the whole São Vicente island.

135 The mineralogy inclusion is done by incorporating the GMINER mineralogical dataset (Nickovic et al., 2012) in the parametrization of the mineral dust aerosol atmospheric life cycle which includes: (1) dust emission following Tegen et al. (2002), (2) aerosol transport (Wolke and Knoth, 2000), and (3) aerosol removal, which includes both dry and wet deposition (Seinfeld and Pandis, 2016; Zhang et al., 2001; Berge, 1997; Jakobsen et al., 1997). Mineral dust aerosols are transported in MUSCAT in five size segregated bins classes and are considered as passive traces, meaning that there is not chemically aging

140 or chemical interaction considered in the simulation.

GMINER follows the Claquin et al. (1999) procedure which extrapolates the mineralogical measurements done for soil classes (following the FAO74 classification (FAO-UNESCO, 1974)) and combines them in order to establish world wide mineral fractions with regards with its soil class in two size classes, namely, clay and silt. The approach is extended in order to consider three new soil types and in particular it extends the hematite fraction to cover both clay and silt sizes. Both extensions

145 result in differences between -0.0007 to 0.08 in the hematite fraction for the studied domain, where the biggest increment of hematite fraction is found in the Sahel following the north-to-south gradient of hematite for the region (Formenti et al., 2014; Scheuvens et al., 2013).

It is evident nonetheless that the uncertainties in the GMINER mineralogical dataset induce errors in calculating the hematite fraction per dust layer. From Fig.1(d) in Li et al. (2024), a comparison between mineralogical datasets and measured iron

150 oxides shows that the Claquin et al. (1999) mineralogical dataset underrepresents under represents the mass fraction of iron oxides for Northern Africa. However, the GMINER dataset by Nickovic et al. (2012) is based on Claquin et al. (1999), but specifically expands the distribution of the hematite content in such a way that agrees with measurements in both silt and clay sizes (Kandler et al., 2009; Wagner et al., 2012). Additionally, the extra soil classifications introduced in GMINER lead to more realistic results through modelling studies (Scanza et al., 2015; Perlwitz et al., 2015a, b). Furthermore, a modelling

155 modeling study comparing mineralogical datasets with in-situ mineralogical aerosol measurements (Gonçalves Ageitos et al., 2023) found that the GMINER dataset better represents the regional variability of emitted iron oxides from North Africa to the Sahel.

While the GMINER dataset does not distinguish between hematite and goethite content, despite both containing iron oxides, their CRI differs between each other in the UV-VIS spectral range (Formenti et al., 2014; Go et al., 2022; Wagner et al., 2012).

160 Chamber studies by Wagner et al. (2012) and Di Biagio et al. (2019) found that goethite has a lower absorption potential than hematite and is weakly correlated with the imaginary part of the dust CRI. Nonetheless, the ~~modelling~~ modeling study by Li et al. (2024) found that considering the separation of dust iron oxide content between hematite and goethite does not significantly alter the global shortwave direct radiative effect. However, since goethite is a big part of the iron oxide content in West Africa (Formenti et al., 2014; Go et al., 2022) and due to the locality of our study region, the lack of distinction between

165 hematite and goethite in the GMINER dataset could impact our results, as the absorption capacity may vary depending on which iron oxide mineral is present in the atmosphere.

An additional source of error arises from the ~~modelling~~ modeling approach of mimicking the mineralogical soil size distribution to the aerosol size distribution, disregarding that the emission process changes the dust size distribution (Marticorena and Bergametti, 1995; Kok, 2011; Journet et al., 2014). This change in size distribution from soil to aerosol mineralogy was

170 specifically observed in the chamber study by Wagner et al. (2012), highlighting the need to incorporate these size distribution changes for upcoming ~~modelling~~ modeling efforts. Although some ~~modelling~~ modeling approaches consider these size distribution changes (Li et al., 2024, 2021; Pérez García-Pando et al., 2016; Perlwitz et al., 2015a, b; Scanza et al., 2015), they all consider the emission parametrization based on Kok (2011)'s brittle fragmentation theory. At present, there is no parametrization that calculates the emission of specific minerals based on Marticorena and Bergametti (1995)'s emission scheme, which is

175 the scheme used in COSMO-MUSCAT.

~~Additionally to~~ Along with the GMINER mineralogical dataset the following input files are used for dust's atmospheric life cycle simulation: dust activation frequency map derived from MSG-SEVIRI IR channels (Schepanski et al., 2007), soil vegetation from Copernicus Global Land Service (Fuster et al., 2020), soil moisture from the ERA5 land hourly data (Muñoz Sabater and Copernicus Climate Change Service, 2019), aerodynamic roughness length data set (Prigent et al., 2005), and soil particle

180 size distribution obtained from the SoilGrids database (Poggio et al., 2021). More information regarding the model setup can be found at Gómez Maqueo Anaya et al. (2024).

For this study, the output used from the model are the vertical profiles of total and size segregated dust mass concentrations and hematite mass concentrations, from which the hematite fraction is obtained by dividing the hematite mass concentration by the total dust mass concentration. The model results are all from above the grid cell corresponding to São Vicente, Cabo

185 Verde for the simulation periods of 8 August - 30 September 2021 and ~~1~~ 2 June - 31 July 2022.

2.2 Polly^{XT}

The lidar data for this study were obtained from an automated multiwavelength Raman polarization and water-vapor lidar, called Polly^{XT} (POrtabLe Lidar sYstem, the XT superscript refers to the updated version) (Althausen et al., 2009; Engelmann et al., 2016). It is part of the Polly^{NET}, which is a network of Polly systems around the world (Baars et al., 2016). This specific

190 Polly^{XT} provides continuous measurements since June 2021 at the OSCM (Ocean Science Center Mindelo) located at Mindelo, São Vicente, Cabo Verde (16°52'39.9"N, 24°59'42.3"W). The produced data from this lidar system has been used for aerosol characterization (Gebauer et al., 2024) and validation purposes (Baars et al., 2023; Gómez Maqueo Anaya et al., 2024). The Polly^{XT} systems emit linearly polarized light pulses at ~~three wavelengths~~ the three wavelengths of 355, 532, and 1064 nm

(covering the UV-IR part of the spectrum); the receiver of the system has fifteen channels, three are used for measuring the backscatter light at the emitted wavelengths, three channels detect cross-polarized light at 355, 532, and 1064 nm wavelengths. The additional four receiver channels ~~for the~~ at 387, 407, 607, and 1058 nm wavelengths are used to detect Raman scattering at nighttime. Signals are measured with a vertical resolution of 7.5 m (1 bin) and a temporal resolution of 30 s. The lidar observations presented here were manually analyzed, a vertical smoothing is necessary to reduce noise in the measurements and facilitate their interpretation. However, the vertical smoothing has been always applied in such a manner that the retrieved values are representing particle values inside the investigated aerosol layer and are not depending on values from outside the aerosol layer. A thorough system description can be found in Gebauer et al. (2024).

The vertical resolved aerosol optical measurements resulting from the lidar signals can be categorized ~~in two general groups~~into two main categories: extensive properties ~~(dependent on the aerosol amount) and intensive properties (independent of the aerosol amount). The measured extensive optical properties are~~ and intensive optical properties. Extensive optical properties, which depend on aerosol concentration, include the particle extinction coefficients (absorption plus scattering) and the particle backscattering coefficients at 355, 532, and 1064 nm wavelengths (α_{355}, α_{532}~~) and backscattering coefficients at 355, 532, and 1064 nm wavelengths (~~, α_{1064} and β_{355}, β_{532}, β_{1064}). ~~The lidar retrieved intensive optical properties are~~ Intensive optical properties, which are independent of aerosol concentration, include the particle linear depolarization ratios at 355, 532 nm and 1064 nm wavelengths (δ_{355}, δ_{532}, δ_{1064}), the ~~backscatter-related~~ extinction-to-backscattering ratio, or lidar ratio, for the UV-VIS wavelengths (S_{355}, S_{532}) and a possibility for obtaining the IR lidar ratio (S_{1064}). The following Ångström exponents are available, backscatter-related, extinction-related and lidar ratio-related for the 355 to 532 nm ~~wavelengths~~ and for the 532 to 1064 nm ~~wavelengths~~ wavelength ranges ($\text{ÅE}(\beta)_{355/532}$, $\text{ÅE}(\beta)_{532/1064}$~~), the extinction-related Ångström exponents for the 355 to 532 nm wavelengths (~~, $\text{ÅE}(\alpha)_{355/532}$~~), and the extinction to backscattering ratio, or lidar ratio, for the 355 and 532 nm wavelengths (S_{355}, S_{532}). The uncertainties related to~~, $\text{ÅE}(\alpha)_{532/1064}$, and $\text{ÅE}(S)_{355/532}$, $\text{ÅE}(S)_{532/1064}$. Uncertainties associated with most of these measurements can be found in Table 1 in Hofer et al. (2017), ~~while detailed discussions regarding them can be found~~ and further discussed in Freudenthaler et al. (2009); Baars et al. (2012, 2016) and Engelmann et al. (2016). Intensive optical properties commonly used for dust characterization as the single scattering albedo or the mass absorption coefficient (Di Biagio et al., 2019; Zhang et al., 2024) cannot be directly obtained from lidar measurements.

The conversion of received signals into optical measurements can generally be done by following one of two methods: the Klett method (Klett, 1985) or a combined Raman elastic-backscatter approach. The Klett method requires an initial estimate of the lidar ratio for the retrievals. In contrast, the Raman method does not require this initial guess, as it allows the independent determinations of the extinction and the backscatter coefficients (Ansmann et al., 1992). Since our focus is on independent lidar ratio measurements, we use only the Raman methodology. However, Raman lidar applications are limited to nighttime measurements because of the necessary inelastic-backscattering signal that can only be detected when the strong daylight background is not there (Ansmann et al., 1992).

Intensive optical properties are ~~used~~ employed for aerosol characterization. Lidar ratios and particle linear depolarization ratios are dependent on particle size, shape, and composition (Hofer et al., 2020; Huang et al., 2023; Miffre et al., 2023; Saito and Yang, 2021; Schuster et al., 2012; Wandinger et al., 2023; Veselovskii et al., 2020)~~, while~~. While the Ångström ~~exponent is~~

mostly exponents are initially believed to be primarly related to the particle size (Ångström, 1929), laboratory and observational studies suggest a substantial dependence of the backscatter-related Ångström exponent on composition, especially when changes in composition lead to variations in the imaginary part of the CRI at UV-VIS wavelengths (Miffre et al., 2020; Veselovskii et al., 20). Under varying conditions, changes in these dependencies affect the optical properties differently, portraying nonlinear relationships between particle physical characteristics and their optical properties.

2.3 Data selection

The selection of aerosol layers intended to study the relation of lidar-measured properties and ~~modelled~~ modeled hematite content focuses on identifying cases where mineral dust was the dominant aerosol. This selection process involves three main, consecutive steps: (1) utilizing AERONET (Aerosol Robotic Network; Holben et al., 1998) measurements to identify potential dust layers, (2) analyzing available Polly^{XT} measurements to confirm these dust layers, and (3) reviewing COSMO-MUSCAT simulation output for the identified cases. An overview of this selection process is illustrated by Fig. 1.

The selection process is constrained by two specific time periods from NH summer measurements campaigns centered around Cabo Verde. The JATAC campaigns, which took place from June to September in both 2021 and 2022, used ground-based, including the Polly^{XT}, aircraft, and balloon measurements to validate data provided by ESA's Aeolous satellite. We decided to focus on these campaigns periods for two main reasons: First, in the spirit of the campaigns' objectives, the data was constantly quality controlled and cross-checked between measurement devices. Second, the summer months are ideal due to the seasonality of Saharan dust transport towards the Atlantic Ocean. During these months, dust travels the highest in the atmosphere (Schepanski et al., 2009) with less interference from other aerosols. Given the data availability of the Polly^{XT} lidar, we narrowed our focus to the following periods for identifying dust-laden aerosol layers: August - September 2021 and June - July 2022.

Within the selected time frame, the next step involved identifying days with dust-dominated aerosol layers. As a first approximation, the total column optical measurements recorded by the AERONET sun-photometer in Mindelo, Cabo Verde, were used. The AERONET level 2.0 (quality-assured and cloud-screened) dataset was then filtered based on the following "pure dust" criteria: Aerosol Optical Thickness ~~(AOT)~~ for the 550 nm wavelength (AOT_{550}) > 0.1 and the exctinction-related Ångström exponent ~~(ÅE)~~ for the 440-870 nm wavelengths $(ÅE(\alpha)_{440/870})$ < 0.3 (Ansmann et al., 2019). As a result of the filtering process, only the dates meeting the "pure dust" criteria remained for the subsequent steps of the selection process.

The second step of the selection process ~~involves~~ involved analyzing Polly^{XT} data. The initial task ~~is~~ was to verify whether the dates that passed the AERONET related filters ~~include~~ included nighttime lidar measurements. The next step ~~is~~ was the manual cloud-screening procedure, as the presence of clouds can influence all particle optical properties~~retrievals~~. If retrievals can be ~~done without clouds interferenceor if there are specific retrieval times where the clouds impact can be minimized~~conducted without cloud interference, or if specific time periods minimize the impact of clouds, the selection process ~~continues~~ proceeded with those suitable times for dust retrievals. When clouds are located below the aerosol layer, they interfere with lidar retrievals targeting the aerosol plume above. This is because multiple scattering within clouds prevents accurate measurement of the aerosol plume. Conversely, if clouds are above the aerosol layer, they do not necessarily contaminate aerosol signals, provided
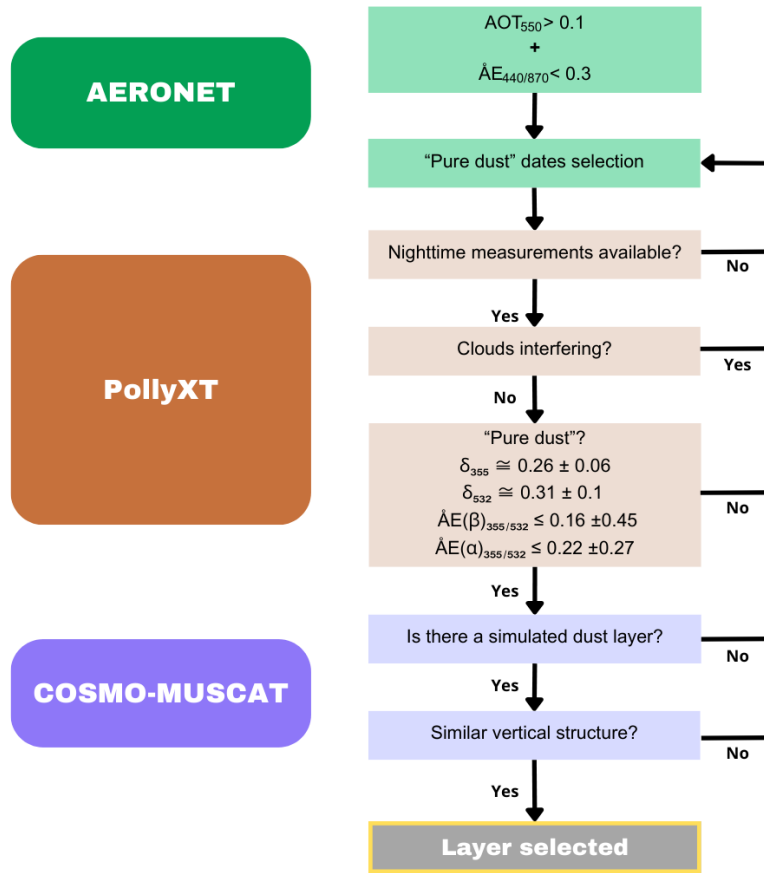
Figure 1. Flow chart of the case selection process. Dust layers are selected through three main steps, the first step is depicted with green colors and relates to date filtering through AERONET measurements and the so-called "pure dust" optical measurements values (Ansmann et al., 2019). The second step is through Polly^{XT} measurements, shown in the figure in orange colors. The first two filters surround the data availability and if clouds are interfering with the measurements while the last filter regards the lidar retrieved optical measurements (Tesche et al., 2011). The third step is pictured in violet colors and it is related to the simulation results from COSMO-MUSCAT, the questions to answer in this section are related to if the dust layer is simulated in a similar way to the lidar vertical structure. Acronyms: Aerosol Optical Thickness at 550 nm wavelength (AOT$_{550}$), extinction-related Ångström exponent for the 440-870 nm wavelengths (ÅE$(\alpha)_{440/870}$), particle linear depolarization ratio at the 355 nm wavelength (δ_{355}), particle linear depolarization ratio at the 532 nm wavelength (δ_{532}), ~~backscattering related~~ backscatter-related Ångström ~~exponent~~ exponents for the 355-532 nm wavelengths (ÅE$(\beta)_{355/532}$), and extinction-related Ångström exponent for the 355-532 nm wavelengths (ÅE$(\alpha)_{355/532}$).

~~there is sufficient separation between the clouds and the aerosol layer. This separation needs to be sufficiently distinct to allow for Raman elastic-backscatter retrievals using a reference height in that intermediate space.~~

265   From this point forward, the selection of "pure dust" days and the nighttime hours from which the vertical optical properties of dust are ~~vertically~~ retrieved from the Polly[XT] measurements has been made. Some "pure dust" days were found to have two distinct dust aerosol layers. Each layer is considered as an individual case study because such layering could be due to atmospheric inversions or to dust originating from different source regions with their own wind pattern, potentially affecting the ~~modelled~~ modeled hematite content between layers. The subsequent step involves selecting dust layers that meet the "pure

270   dust" criteria based on lidar optical measurements, excluding considerations for lidar ratios. The criteria, based on Tesche et al. (2011), are as follows: $\delta_{355} \simeq 0.26 \pm 0.06$, $\delta_{532} \simeq 0.31 \pm 0.1$, $\text{ÅE}((\beta)_{355/532}) \leqslant 0.16 \pm 0.45$, $\text{ÅE}((\alpha)_{355/532}) \leqslant 0.22 \pm 0.27$ ~~.~~ ~~As illustrated in step 5 of~~ as illustrated in the last subsection of the Polly[XT] step in Fig. 1.

The third step of the selection process takes into account the COSMO-MUSCAT modelling results. The first criterion is whether the model simulates the dust layer(s) for the same date and time where the dust layer(s) were ~~measured~~ observed by

275   the Polly[XT]. If this criterion is met, the next step is to assess if the model reproduces a similar vertical structure. A dust layer is selected for ~~the~~ this study if the model both simulates the dust layer(s) at the corresponding dates and times and simulates a comparable vertical structure. Between 19-08-2021 and 08-07-2022, 22 dust layer ~~(s)~~ cases passed the data selection filters.

2.4 Layer comparison

The comparison between the vertically resolved optical property, the lidar ratio, at both 355 nm and 532 nm wavelengths and

280   the ~~modelled~~ modeled hematite fraction is ~~shown~~ illustrated in Fig. 2 for a hypothetical case based on lidar and model data. This comparison is done for each dust layer, where a mean value is calculated based on their own vertical structure. Specifically, the optical properties means are calculated by taking into account the thicknesses of each dust layer as retrieved by Polly[XT], while the hematite fraction means are calculated based on the thickness of each COSMO-MUSCAT simulated dust layer. For instance, for the two dust layers sketched in the Fig. 2, one mean lidar ratio value at 355 nm and another at 532 nm are

285   calculated for the dust layer in between ~~1.5 and 2.8~~1.4 and 3 km. These values are then compared to the mean hematite fraction (hematite mass concentration divided by the total dust mass concentration) for the simulated dust layer in between ~~1 and 3~~0.9 and 2.8 km. For the lofted layer, the lidar ratio means are computed for the range between ~~3.6~~3.7 and 5.2 km and are compared with the ~~modelled~~ modeled mean hematite fraction in the range of 3 to 5.3 km.

2.5 POLIPHON

290   The two-step POLIPHON method (Mamouri and Ansmann, 2014, 2017) translates lidar-retrieved optical properties into mass concentrations of coarse dust (particle diameter (D) > 1 µm), fine dust (D < 1 µm), and non-dust concentrations. This separation is achieved ~~using the measured particle linear depolarization ratio and involves three main steps, considering the~~ by utilizing the lidar retrieved δ ~~values for the separations~~ and β values, AERONET-derived conversion factors, and assumed values for S and ~~densities are based on both Ansmann et al. (2019) and Mamouri and Ansmann (2017): Separation of particle~~

295   ~~backscatter coefficient: The initial step involves separating the particle backscatter coefficient based on~~ density. The method
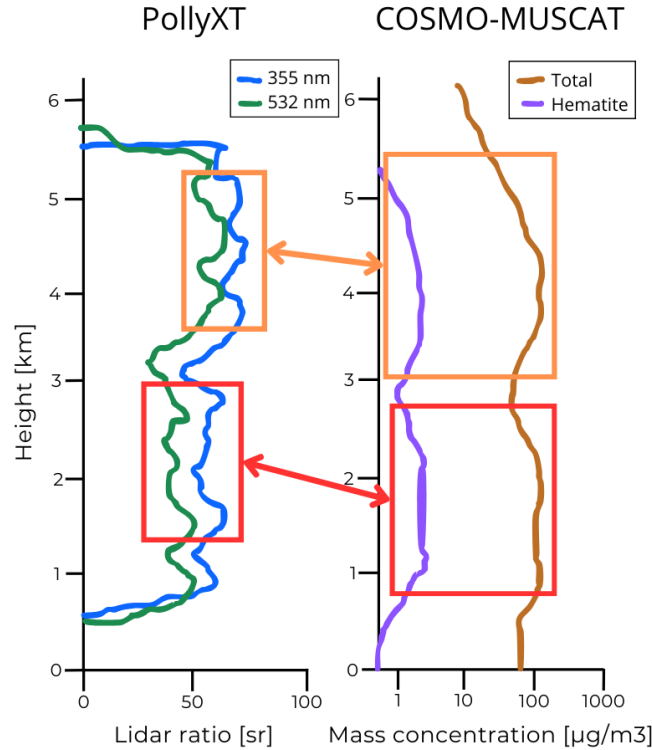
Figure 2. Sketch illustrating how the dust layers are compared between the Polly[XT] results and the COSMO-MUSCAT simulated dust layers. On the left hand side the lidar ratio vertical structure is sketched for the 355 nm (blue) and 532 nm (green) wavelengths. On the right hand side, the vertical structure of the ~~modelled~~ modeled total dust mass concentration (brown) and hematite mass concentration (purple) are sketched. The boxes represent the domain of one dust layer and the arrows represent relation between the measurements. The sketch represents dust related vertically distributed properties above Mindelo, São Vicente, Cabo Verde.

involves the ~~particle linear depolarization ratio. This step~~ separation of the measured β values using the retrieved δ values to estimate α values based on assumed S values, and afterwards, converting the calculated particle extinction coefficients into mass concentrations by applying the AERONET-derived conversion factors and an assumed densities (ρ). The specific values used for the dust layers analyzed in this study are provided in Table 1. The two-step POLIPHON processes are described in

300 detail below.

    Separation of particle backscatter coefficient: this procedure consists of two processes:~~first~~. Initially, a broad separation between coarse dust and the mixture of fine dust and non-dust aerosols is performed based on δ values (Fig. 3b). Defined threshold values of δ are compared to the lidar retrieved δ values to achieve this separation. For this first step, the δ values for coarse dust, as listed in Table 1, is applied, together with the fine dust ~~is performed, and then the fine dustfraction is further~~

305 ~~divided into fine dust~~ and non-dust ~~fractions. Calculation of particle extinction coefficient: In the second step, an extinction coefficient is derived from the separated particle backscatter coefficients. This requires estimating the lidar ratio~~ mixture δ

value. In this study, a δ value of 0.12 is used for the mixture of fine dust and non-dust, as the analyzed dust layers are located above the marine boundary layer, where non-dust aerosols are primarily of a continental nature (Mamouri and Ansmann, 2017).

310 The second process separates fine dust from non-dust aerosols using δ threshold values fo these categories, as shown in Table 1. Ultimately, the values of β for coarse dust, fine dust, and non-dust are determined. Then δ threshold values used for the separation of non-dust and dust categories are derived from extensive lidar measurements (Mamouri and Ansmann, 2014), while the coarse and fine dust δ values are obtained from laboratory studies (Sakai et al., 2010 and Järvinen et al., 2016, correspondingly). Additionally, the δ values assigned to the fine dust and non-dust mixture depend on the nature of the non-dust aerosol and is determined iteratively by comparing the results it yields with lidar measurements, as detailed in

315 Mamouri and Ansmann (2014, 2017).

Calculation of particle extinction coefficient: once the backscatter coefficients are separated, α is calculated by applying appropriate lidar ratio values for each fraction~~, with the~~. The same S ~~value used~~ values are assumed for dust-related fractions ~~. The extinction coefficient (α) is calculated by multiplying the segregated backscatter coefficients (β) by their corresponding~~

320 ~~lidar ratios. The lidar ratios are estimated~~ while the non-dust value is based on the likelyhood of the aerosols origin. The estimates are based on regional data and ~~the probable origins of non-dust aerosols (e.g., marine or continental). Conversion to mass concentrations: The final step involves converting the calculated extinction coefficients (α)~~ are derived from an extensive collection of previous lidar observations (Mamouri and Ansmann, 2014, 2017). The extinction coefficient is obtained by multiplying the separated β by their corresponding S values.

325 **Conversion to mass concentrations:** the extinction coefficients are then converted into volume concentrations ~~and then~~ using specific conversion factors, followed by the transformation into mass concentrations ~~using~~ through the application of appropriate density values. ~~Conversion factors for this transformation, determined~~ These conversion factors are derived from AERONET aerosol climatologies~~(Mamouri and Ansmann, 2014, 2017; Ansmann et al., 2019), are applied.~~

~~Several assumptions are included in the POLIPHON method~~, ~~most notably the homogenization~~ while the assumed densities

330 are based on previous aerosol studies and the assumption of homogeneity within dust and non-dust categories (Ansmann et al., 2012, 2019).

The POLIPHON method incorporates several assumptions, the most notable being the uniformity of optical properties ~~values~~ across all mineral dust particles, ~~which disregards the~~ disregarding variations due to different ~~dust~~ source regions. However, a significant ~~advantages of this method~~ advantage of this approach is that it does not require a dust particle shape model ~~in~~

335 ~~the data analysisince it relies~~ for data analysis, relying solely on the measured optical properties. ~~Additionally, this method~~ Nevertheless, since the method involves a conversion factor based on AERONET climatologies, it is important to note that in order for AERONET to derive aerosol mass fractions, a spheroid shape assumption is used (Dubovik et al., 2006). The two-step POLIPHON method has been validated, ~~since good agreement was found~~ demonstrating good agreement between airborne measurements and lidar retrieved, two-step POLIPHON derived, fine and coarse modes of dust mass concentrations

340 on Barbados during the SALTRACE campaign (~~Fig. 5 in~~ Haarig et al., 2019).

Table 1. Used values for implementing the two-step POLIPHON method. Values are obtained from Ansmann et al. (2019, 2012); Mamouri and Ansmann (2017). δ is the particle depolarization ratio, S is the lidar ratio and C_v is the volume conversion factor, and ρ represents density. Units in square brackets.

Parameter	Non-dust	Dust	Coarse dust	Fine dust
δ	0.05	0.31	0.39	0.16
S	50	50	50	50
C_v [10^{-12}Mm]	0.22±0.06	0.64±0.07	0.79±0.08	0.22±0.06
ρ [g/cm^3]	1.5	2.6	2.6	2.6

The ~~data produced from the POLIPHON~~ two-step POLIPHON derived data are employed in this study as an ~~analysis tool . Two key ratios are used for that purpose: first~~analytical tool with two key mass concentration ratios serving specific purposes. First, the ratio of non-dust to dust mass concentration is used ~~for color-coding each~~ to color-code each dust layer case and for quantifying relationships between different case studies. Second, the ~~ratio of~~ fine-to-coarse dust mass ~~concentrations~~ concentration ratio is used to categorize the case studies into three distinct groups: (1) dust layers with a higher portion of fine dust mass concentration (i.e., fine/coarse > 11%), (2) dust layers with ~~intermediate amounts~~ an intermediate proportion of fine dust mass concentrations (i.e., 9% < fine/coarse < 11%), and (3) dust layers with a lower portion of fine dust mass concentration (i.e., fine/coarse < 9%). It is important to ~~note~~ emphasize that this classification is specific to ~~these case studies~~ the analyzed cases and does not ~~imply a general classification of what it means for a dust layer to have a~~ represent a universal standard for defining "~~large~~high" ~~proportion of~~ fine-to-coarse dust mass ~~concentrations ratio. The rationale for this division is based on the~~ concentration. Moreover, considering the uncertainties associated with mass concentrations calculations, 20 - 30% for total mass concentration, 40 - 60% for the fine-mode mass concentration, and 25 - 35% for coarse-mode mass concentration (Ansmann et al., 2019), the proposed classification falls outside the uncertainty margin. Therefore, these divisions should be regarded as exploratory and artificial, intended solely for the purposes of this study. The primary objective is to investigate a potential method for disentangling physical parameters influencing intensive optical properties, particularly in light of the evident impact of dust ~~size on lidar ratio measurements~~particle size on the lidar ratio, as shown in Fig. 5 in Wandinger et al. (2023) and Fig. 15 in Zhang et al. (2024). ~~Additionally, the~~

Additionally, to support the validation of model results, the fine-to-coarse dust mass concentration ratio derived from the POLIPHON is compared with the corresponding ratio from COSMO-MUSCAT ~~per dust layer~~to enhance for each dust layer. This comparison enhances the reliability of the ~~comparative analysis between model and lidar measured data~~analysis by providing a more robust assessment of model and lidar-derived data agreement. The described products and their application are illustrated in Fig. 3.
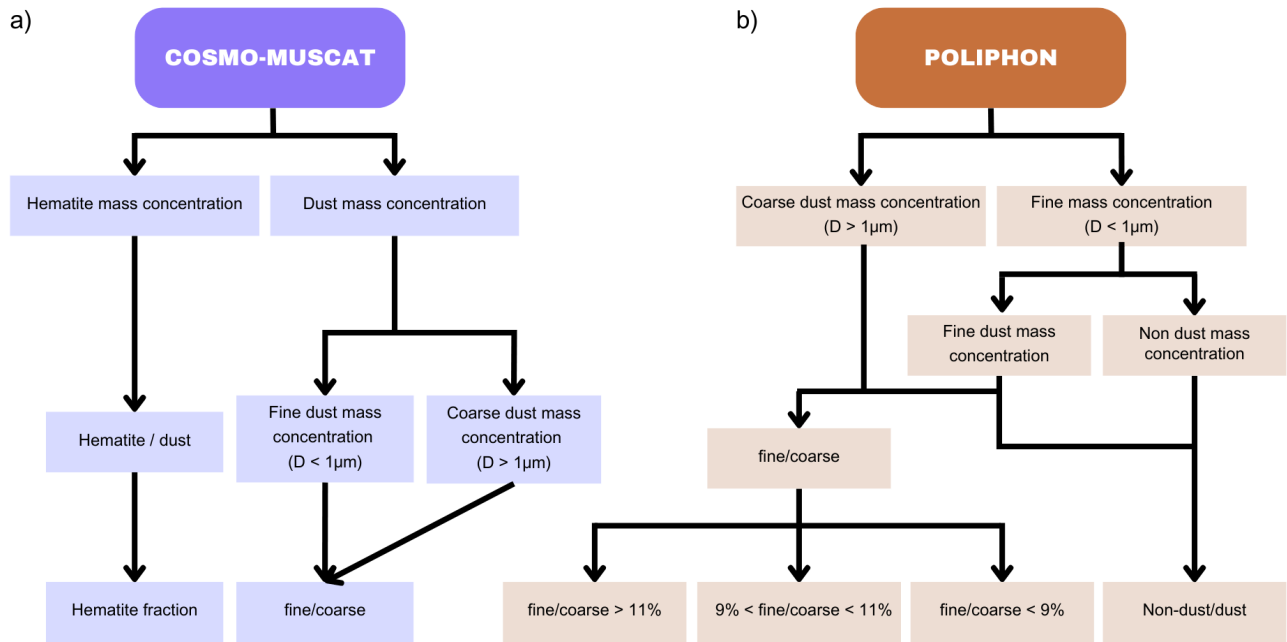
Figure 3. Process flow illustrating two main methods and their corresponding data outputs used in the study. (a) Violet colors represent the output from COSMO-MUSCAT. The fine-to-coarse dust mass concentration ratio, and hematite fraction are the model output products used for the results. The particle diameter threshold for distinguishing between fine and coarse dust mass concentration is set at 1 μm to align with the POLIPHON classification. (b) The POLIPHON output flow is shown in orange colors. The products from the POLIPHON used for the results are the fine-to-coarse dust, and the non-dust to dust mass concentration ratios.

3 Results and their discussion

This section is structured as follows: First, lidar measurements from ~~a single day~~ 24 August 2021 are shown and described. On this day, two distinct dust layers are identified and analyzed as separate case studies. The dust layers are shown after applying the 2-step POLIPHON method, and the results are compared with the corresponding COSMO-MUSCAT results for the same day and time. Next, the bulk of case studies is presented, beginning with a comparison of the fine-to-coarse ratios derived from COSMO-MUSCAT and POLIPHON. This is followed by an analysis of the relationship between hematite fraction and lidar ratio, as well as particle linear depolarization ratio at both at 355 nm and at 532 nm, and backscatter and extinction-related Ångström exponents. Finally, ~~for~~ the cases analyzed separately according to size, the hematite ~~fraction is~~ fractions are compared with the aforementioned lidar-measured optical properties.

Table 2. Mean values of lidar ratios (S), particle linear depolarization ratios (δ), backscatter-related Ångström exponent ($\text{ÅE}(\beta)$) and extinction-related Ångström exponent ($\text{ÅE}(\alpha)$) for the 355 nm and 532 nm wavelengths for two dust layers measured on 24 August 2021, 02:45-05:27 UTC. Reference "pure dust" values from Tesche et al. (2011) on the last row.

Height	S_{355} [sr]	δ_{355}	S_{532} [sr]	δ_{532}	$\text{ÅE}(\beta)_{355/532}$	$\text{ÅE}(\alpha)_{355/532}$
1.4 - 2.1 km	59±6	0.201±0.012	44±10	0.252±0.007	-0.26±0.05	0.54±0.57
2.7 - 5.2 km	61±5	0.236±0.003	48±4	0.292±0.001	-0.49±0.07	0.08±0.34
~~Tesche et al. (2011)~~ "pure dust" following Tesche et al. (2011)	53±10	0.26±0.06	54±10	0.31±0.1	0.16±0.45	0.22±0.27

3.1 Single case study - 24 August 2021

3.1.1 Observed dust optical properties

Figure 4 shows the vertical distribution of optical properties retrieved from Polly$^{\text{XT}}$ on the 24 of August 2021 between 02:45 UTC and 05:27 UTC. The vertical profiles show two aerosol layers. In order to accurately determine their heights, a lower vertical smoothing is used to enhance the distinction between aerosol layers and air layers with less particle contents. The heights of the layers are then set using a vertical smoothing of 22.5 m~~(3 bins; profiles not shown)~~. By cross-checking the measured optical properties against the values signaling for dust layers (Tesche et al., 2011) in Cabo Verde (step ~~5~~ 2 of Fig. 1's flow chart), it is confirmed that the measurements for this day correspond to two distinct dust layers, each to be considered as a separate case study (see Table 2). The vertical smoothing used to calculate their optical properties is different for the layers to balance the number of independent measurements and the length of their standard variation. For the lower layer near the surface, a vertical smoothing of 232.5 m ~~(31 bins)~~ is applied, while for the upper layer, a vertical smoothing of 577.5 m ~~(77 bins)~~ is used, ~~as~~ which profiles are illustrated in Fig. 4. It is noteworthy that the particle backscatter coefficient shows a wavelength dependence, with larger β values for 532 nm than at 355 nm for the upper dust layer but not for the lower layer. The mean values of the particle extinction coefficient fall within their measurement error margins when comparing 355 nm to 532 nm wavelengths across both dust layers, implying wavelength independence. Such ~~behaviour~~ behavior is not uncommon for Saharan dust (Veselovskii et al., 2016, 2020). Since our study focuses on the optical properties of dust independent from the amount of it, with particular interest in ~~absorption~~ backscattering characteristics, the emphasis is in the intensive optical properties. Table 2 provides the mean values of these intensive optical properties for each dust layer together with Tesche et al. (2011)'s reference "pure dust" values.

The mean values of the intensive optical properties reveal that the lidar ratios at 355 nm fall within the upper half of the "pure dust" tolerance range, whereas the lidar ratios at 532 nm are in the lower half of this range. For the particle linear depolarization ratios, the values at 355 nm are in the lower half of the "pure dust" tolerance range, while the values at 532 nm are within the inner half of the "pure dust" tolerance range. The backscatter-related Ångström exponent values are either on the lower end (lower layer) or below the lower limit of the specified range (upper layer), whereas the extinction-related Ångström exponent
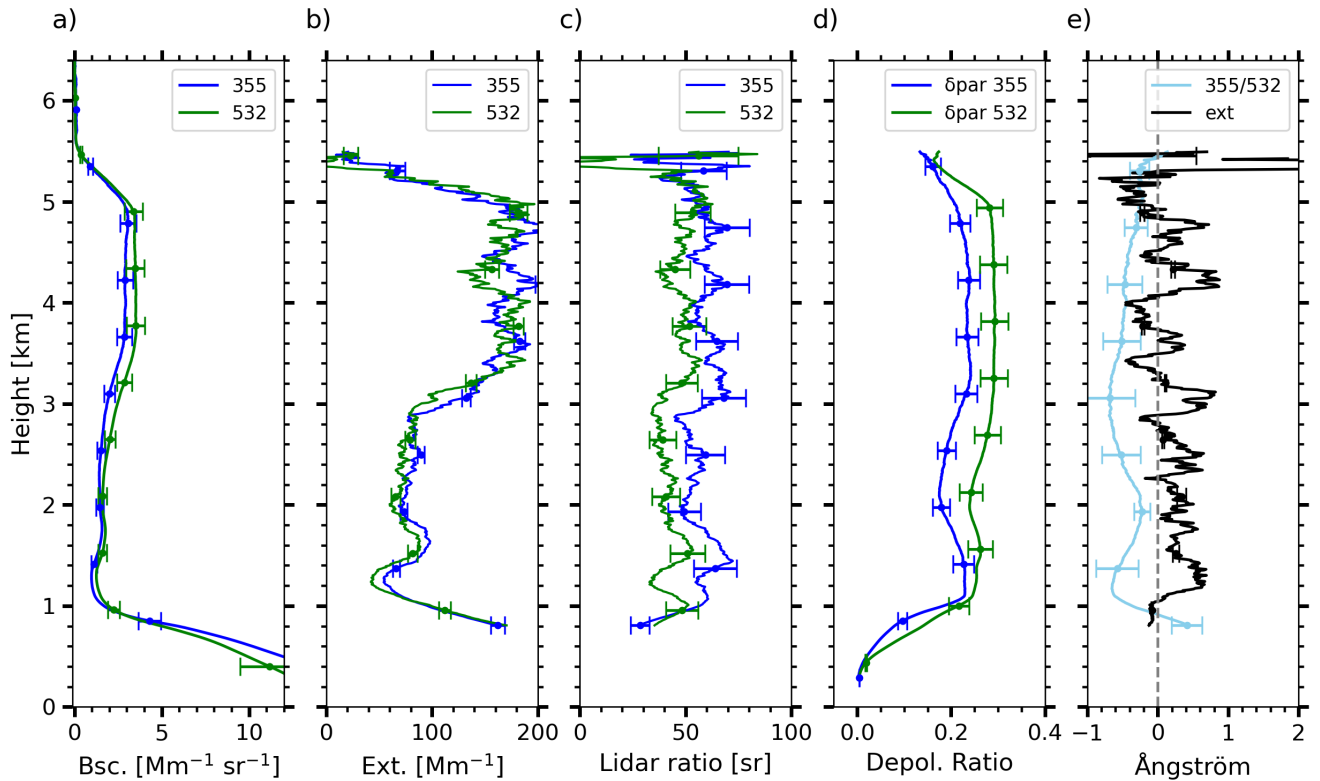
Figure 4. Average lidar profiles measured on 24 August 2021, 02:45-05:27 UTC. The vertical profiles are vertically smoothed before calculation with a resolution of 577.5 m. For plots (a-d), blue represents measurements at 355 nm and green represents measurements at 532 nm wavelength. The optical properties shown are: particle backscatter coefficient (Bsc. (β)) (a), particle extinction coefficient (Ext. (α)) (b), lidar ratio (S) (c), and particle linear depolarization ratio (Depol. ratio (δ)) (d). For the Ångström ~~exponent~~ exponents (~~Ångström (~~ÅE) ~~)~~ plot (e), both ÅE shown are calculated for the 355-532 nm wavelengths, the backscatter-related ÅE is shown in light blue and the extinction-related ÅE is shown in black.

values are either above the upper limit of the "pure dust" range (upper layer) or on the lower limit of the specified range (lower layer). Values close to zero for both ÅE(β) and ÅE(α) are related ~~with~~ to the presence of large particles. Negative values are not unusual for Saharan dust (Haarig et al., 2022; Veselovskii et al., 2016, 2020), with measurements showing ÅE(β) ranging from -0.55 to 0.5 and ÅE(α) ranging from -0.2 to 0.2. Negative ÅE(β) values can result from a spectral dependence on changes in the imaginary part of dust's CRI at ~~355 nm~~UV-VIS wavelengths. A sensitivity study performed in Veselovskii et al. (2020) shows that the ÅE(β) is more affected than ÅE(α) by changes of the imaginary CRI part at 355 nm, as it decreases while the imaginary part increases. The increase of S values, along with the changes in ÅE(β) between lower and upper layer, suggest that these differences may be influenced by a mineral, such as hematite, that ~~increase~~ increases the imaginary part of the dust's CRI at the UV-VIS spectral range.

3.1.2 POLIPHON derived vs COSMO-MUSCAT dust concentrations

The results from applying the two-step POLIPHON method to measurements from 24 August 2021, alongside COSMO-MUSCAT simulation results for that same day at a similar time range (3:00-6:00 UTC) are presented in Fig. 5. The COSMO-MUSCAT simulation results depicts a two dust layer structure; however, the altitudes of these layers do not align precisely with those observed. For comparison purposes, the COSMO-MUSCAT dust layers are defined as follows: lower layer extends from 0.8 to 2.7 km, while the upper layer ranges from 3 to 4.8 km.

According to the POLIPHON results, the average dust mass concentration in the lower layer is 118 µg/m^3, while the upper layer reaches 270 µg/m^3. COSMO-MUSCAT simulation estimate an average dust mass concentration of 179 µg/m^3 for the lower layer, and 97 µg/m^3 for the upper layer. This indicates that the model overestimates the dust concentration in the lower layer by a factor 1.5 and underestimates it in the upper layer by a factor of 0.35. Despite these discrepancies, the model fits well to the total measured dust mass load. This can be seen in the good agreement between AERONET and COSMO-MUSCAT total column AOT for the Mindelo station on 23 August 2021 at 19:00 UTC, where the model calculates a total column AOT of 0.84, while AERONET measurements show an AOT of 0.76 (Fig A1).

Regarding the fine-to-coarse dust ratio, POLIPHON derived values indicate an average of 0.15 for the lower layer and 0.08 for the upper layer. COSMO-MUSCAT simulates a ratio of 0.1 for the lower layer and 0.12 for the upper layer. The model simulates coarser particles for the layer closer to the ground, which may explain the higher modeled dust mass concentration for that layer. Conversely, the model estimates a greater fraction of fine dust in the upper layer compared to observed, which may contribute to the underestimation of mass concentration at those altitudes. Despite these discrepancies, the model effectively represents the two-layer dust structure, and the two datasets are sufficiently well related, as the mass concentrations are of the same order of magnitude. This level of agreement allows for a meaningful combined analysis, particularly since the focus of this study is on mass-independent properties. It is noteworthy that the discrepancies may also stem from the model averaging the dust plumes across the entire island, making it inherently unable to capture the exact same vertical structure that is observed by lidar measurements.

Furthermore, the average hematite fraction per dust layer is 0.008 for the lower layer and 0.011 for the upper layer. These results support the assumption that an increase on the hematite fraction may have affected the measured intensive optical measurements between the dust layers. However, the lidar ratio values for this case are too similar to definitively attribute any difference due to hematite presence. In contrast, a clear increase in the ÅE(β) is observed between the layers, suggesting a potential influence of hematite on this parameter.
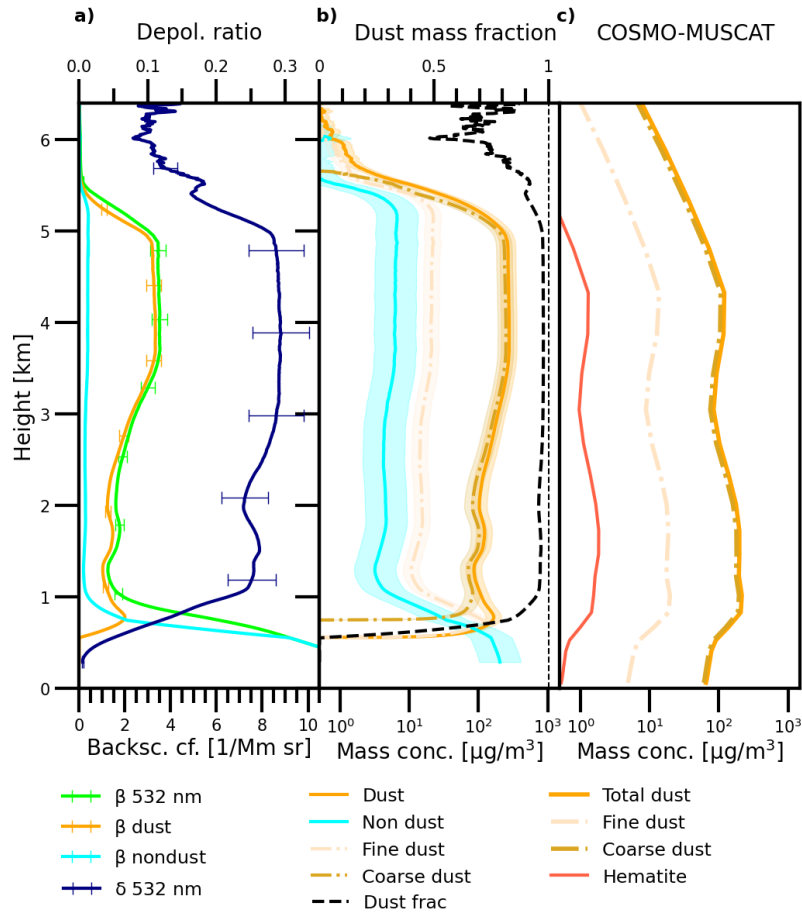
Figure 5. Vertical profiles for the POLIPHON derived products from lidar measured optical properties on 24 August 2021 02:45-05:27 UTC, and COSMO-MUSCAT simulation results above Mindelo. The 532 nm particle backscatter coefficient (a, light green) and the particle linear depolarization ratio (a, dark blue) are the input to obtain the separated dust and non-dust profiles in (a, b). The POLIPHON products are the derived 532 nm dust backscatter coefficient (a, orange) and the non-dust backscatter coefficient (a, light blue), dust mass concentration (b, orange), coarse dust mass concentration (b, gold), fine dust mass concentration (b, bisque), the non-dust mass concentration (b, light blue), and the dust mass fraction (b, black, ratio of the dust to total particle mass concentration, dashed black vertical line indicates a dust mass fraction of 1). Vertical profiles of simulated mineral dust mass concentrations from the COSMO-MUSCAT model (c). The vertical profile corresponds to values calculated for the grid cell where Mindelo, Cape Verde is found in the model for 24 August 2021 3:00-6:00 UTC. Total dust mass concentration (c, orange), coarse dust mass concentration (c, gold), fine dust mass concentration (c, bisque), and hematite mass concentration (c, tomato) are shown.
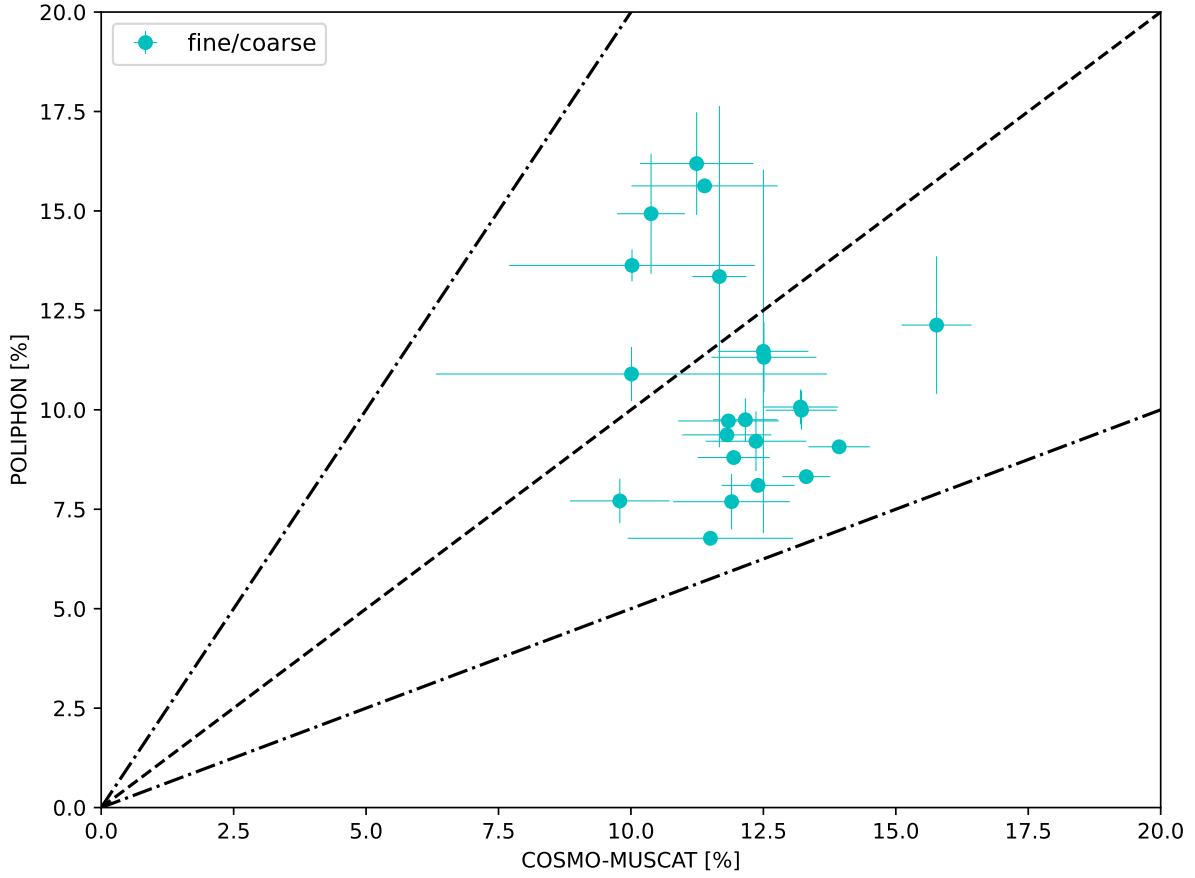
Figure 6. Fine-to-coarse dust mass concentrations comparison between COSMO-MUSCAT and POLIPHON. The dashed line represents the 1:1 line and the dash-dot lines represent the 2:1 and 1:2 lines. The error bars represent the standard deviation of the ratio per dust layer.

3.2 Multiple case studies

Figure 6 shows the fine-to-coarse dust mass concentration ratios obtained from POLIPHON compared to the COSMO-MUSCAT simulation results for 22 case studies. The results show that the ratios are in the same order of magnitude and they all fall within the range of the 2-to-1 and 1-to-2 lines. There is a notable tendency for COSMO-MUSCAT to lean towards the 2-to-1 comparison, indicating a slight overestimation of the fine portion of the dust mass concentration.

Studies by Adebiyi and Kok (2020) and Kok et al. (2017) compared ensembles of atmospheric models with dust aerosol in-situ measurements and found that atmospheric models tend to ~~ovepredict~~ over predict the fine dust portion while underestimating the coarse dust portion. This over and under prediction has impacts on the calculation of the global direct radiative effect. Fine dust significantly contributes to the extinction at 550 nm, with only a few percent of that extinction due to absorption, whereas coarse dust absorbs a larger fraction of the extinguished radiation at 550 nm (Adebiyi et al., 2023).

To further validate the model results, a comparison of the aerosol mass loading was conducted by analyzing total column aerosol optical thickness (AOT) at 550 nm against AERONET data. This comparison considered five AERONET stations strategically distributed across the Sahara Desert region and along the dust transport pathway over the Atlantic, with corresponding grid cells values in the model results. Despite certain limitations, such as extended periods of missing data for some stations, and specific events being misrepresented by the model, COSMO-MUSCAT effectively reproduces the temporal evolution of dust plumes in the region, capturing the general patterns of timing and intensity, particularly for the periods of time when the $\text{ÅE}(\alpha)_{440/870}$ are below 0.3, indicating that dust is the the main aerosol type.

These findings suggest that the model captures well the dust transport across the region. Furthermore, considering that dust plumes during this season typically travel above the marine boundary layer (Schepanski et al., 2009), the dust observed over Cabo Verde is mostly part of the larger regional transport patterns rather than originating from local emissions. The results are presented and further discussed in the Appendix A.

3.2.1 Dependence of optical properties on hematite fraction

Figure 7 illustrates the ~~relationship between the average modelled hematite fraction and lidar retrieved intensive optical properties across the 22 study cases. The linear fits for the lidar ratio changes in relation to increases in the hematite fraction reveal a weak to non-existent relation, indicating that the changes in the hematite fraction do not linearly impact lidar ratio values for either the 355 or the 532 nm wavelength (Fig. 7(a) and Fig. 7(b)). The Pearson correlation coefficient and p-value for the S_{355} and hematite fraction show a very weak positive relationship (r=0.09)with no statistical significance (p=0.68), while for the S_{532} case, the values depict a moderate positive relationship (r=0.36), but also lack statistical significance (p=0.1). The Pearson correlation coefficients and p-values for the~~ relationship between the ~~particle linear depolarization ratios and hematite fractions show no significant relations, with p-values above or equal to 0.95. However, the correlation coefficients for the relationship with the~~ average modeled hematite fraction and lidar retrieved intensive optical properties across 22 dust layers. While no significant correlation is found between hematite fraction and lidar ratios or particle depolarization ratios at 355 and 532 nm, indicating a limited influence of hematite content on these properties, a moderately positive correlation is observed between the backscatter-related Ångström exponent ~~, both for the backscatter-related~~ (ÅE~~and the extinction ÅE show moderately positive relationships (r~~$(\beta)_{355/532}$) and hematite fraction (R^2~~=0.41 and r=0.39)with marginal statistical significance (p=0.06 and p=0.07)~~0.49). This suggest that hematite fraction influences dust backscattering properties with a wavelength dependence, leading to higher backscattering coefficients at 532 nm compared to 355 nm.

The color coding in the lidar ratio analysis in Fig. 7 represents the fine-to-coarse fraction in percentage. ~~In Fig. 7(a), the point~~ Noteworthy, the points with the highest fine-to-coarse fraction (16%), shown in yellow, ~~lies~~ lie outside of the range of the other S_{355} ~~values. In contrast, Fig. 7(b) does not show a clear influence of this fraction on S_{532}.~~ S values. Lower fine-to-coarse percentages are clustered around hematite fractions of 0.01 to 0.012.

~~In summary, there is no statistically significant relationship between the~~

Limited correlations between most measured intensive optical properties and ~~the modelled hematite fractions per dust layer. This lack of correlation~~ modeled hematite fractions are observed. This is likely because of the ~~lidar ratio depending non-linearly~~
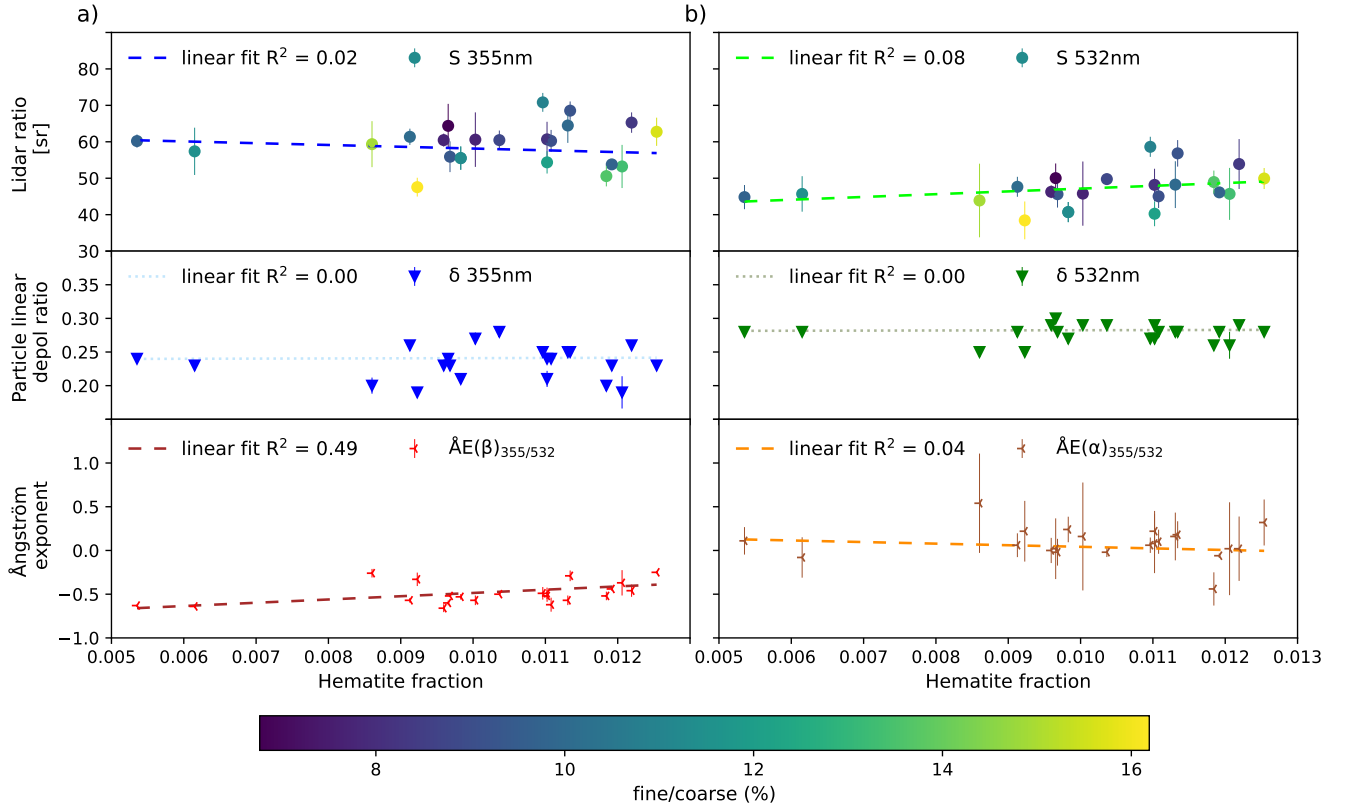
Figure 7. Mean values for 22 dust layers, hematite fractions are shown in the x axis and three intensive optical properties are shown in the y axes per graph. Lidar ratios are shown in color coded dots, its standard deviation is shown by the error bar. The triangle symbols represent the particle linear depolarization ratios with is standard deviation in the error bar, and the Ångström exponents are depicted by the 45° tilted "Y" symbols. Linear fits between the hematite fraction and the intensive optical properties are illustrated by the dotted lines, the R squared value of the linear fit is shown in the dashed line legends. (a) Illustrates S_{355}, δ_{355}, and $\text{ÅE}(\beta)_{355/532}$, (b) shows the values related to S_{532}, δ_{532}, and $\text{ÅE}(\alpha)_{355/532}$. The color coding of the lidar ratio depends on the fine-to-coarse fraction obtained from the POLIPHON method, values in percentage are shown by the color bar.

~~to~~ nonlinear dependence of these intensive optical on particle size, shape and composition (Huang et al., 2023; Saito and Yang, 2021; Wandinger et al., 2023). Studies by Di Biagio et al. (2019) and Adebiyi and Kok (2020) indicate that the absorption efficiency increases with particle diameter, while the scattering efficiency decreases. ~~Therefore, it is recommended to separate the~~

485 ~~study cases by~~ To better understand these dependencies, separating study cases based on the fine-to-coarse ~~ratio to disentangle these dependencies. Additionally, it is important to note that although the study cases were carefully selected~~ particle ratio is recommended, in order to ~~isolate dust dominated aerosol layers, other aerosols that can affect the measured optical properties may still be present. For example, aerosols that are a product~~ control for big variabilities in the particle size distribution from one dust layer to another.

490 Furthermore, the lidar ratio related Ångström exponent for the 355 and 532 nm wavelengths ($\text{ÅE}(S)_{355/532}$) exhibits a weak negative correlation with hematite. This suggests that the hematite fraction may influence the lidar ratio with a wavelength dependence, potentially by impacting more S_{355} than S_{532}. This influence could be attributed to the effect of hematite on the imaginary part of the CRI through its impact of dust absorption and/or backscattering properties. However, with a low R-squared value of 0.25, this relationship remains weak and non-significant to provide any conclusions (see Fig. B1).

495 While for this study dust-dominated layers were carefully selected, the presence of other aerosols, such as those from anthropogenic activity, e.g., black carbon ~~,~~ and biomass burning ~~are known for absorbing~~, cannot be entirely ruled out. These aerosols, particularly black carbon, are known to absorb radiation, specially in UV part of the spectrum (Li et al., 2022; Tesche et al., 2011)~~.~~, which can potentially influence the measured optical properties. However, we minimized the potential impact by applying the $\text{ÅE}(\alpha)_{440/870}$ criterion for the dust layer selection (see step 1 in Fig. 1).

500 Interestingly, the observed moderately linear relationship between $\text{ÅE}(\beta)_{355/532}$ and hematite fraction is not reflected in the lidar ratio analysis. This is partly explained by the lack of correlation with the extinction-related Ångström exponent ($\text{ÅE}(\alpha)_{355/532}$), thereby diminishing the influence of hematite on dust backscattering properties. Beyond compositional changes, intensive optical properties also depend on shape and size. Given the methodology used for this study, an intriguing opportunity is presented in order to explore whether limiting size variations within the dust plumes could potentially strengthen correlations

505 between hematite fraction and intensive optical properties.

3.2.2 Size dependency

To gain a clearer understanding of the relationship between the measured intensive optical properties and the ~~modelled~~ modeled hematite fraction, the study cases were separated into three artificial clusters based on different fine-to-coarse dust mass ratio ~~. This approach is made with regards to the idea that reducing size changes~~ (see Fig. 3). This clustering approach aims to

510 reduce size variations within the dust layers ~~would mitigate the~~, mitigating the size-dependent effects of the lidar ratio ~~'s size dependency~~ and the backscatter-related ÅE.

Figure 8 shows ~~dust cases separated according to size differences and~~ the cases segregated by size differences, while Table 3 ~~shows~~ summarizes the mean values per size class of the intensive optical properties and their ~~Pearson~~ correlation coefficients. In Fig. 8(a-b) ~~shows~~ the cases with the highest fine-to-coarse ratios are shown, reflecting larger proportions of fine and, ~~indicating~~

515 ~~a larger portion of fine dust portion and~~ therefore, the cases where the particle sizes change the most consequently, the greatest

particle size variations within a dust layer. Fig. 8(e-f) ~~illustrates~~ depicts cases with the largest coarse dust portion, ~~implying less size variations~~indicating less drastic size variations within each dust layer, while Fig. 8(c-d) represents the intermediate cases.

~~Analysis of the linear fits~~ Linear regression analysis revealed that for these cases ~~suggest that~~ a linear model does not adequately explain the data variability of most of the optical properties analyzed. Nevertheless, ~~it is noteworthy that both the R², and the Pearson correlation coefficients (r and p)change positively from~~ the correlations with the backscatter-related ÅE are consistently significant, with the highest correlation coefficient found in the intermediate size cluster Fig. 8(c). Notably, the correlation coefficient, R^2, increases positively when moving from cases with the higher fine dust portion ~~towards those with less.~~to those with lower proportions, as seen in Fig. 8(a,b) compared to Fig. 8(e,f), suggesting a stronger relationship between hematite fraction and backscattering properties in coarser dust layers. This clustering approach is validated by the observed mean values. Due to the influence of coarser particles in the lidar ratio, it is expected that the values of S for coarser particles are higher than those associated with finer particles. This effect is evident in the size clustering, as reflected in the mean values summarized in Table 3.

For the relationship between hematite fractions and S_{355} Fig. 8(a,c,e), ~~the Pearson correlation coefficients and p-values shift from a very weak negative relationship with no statistical significance (r=-0.03, p=0.94), to a moderate positiverelationship with a lack of statistical significance (r=0.46, p=0.36). For~~ correlation coefficients shift from non significant to moderately positive. Similarly, for the relationship between hematite fractions and S_{532} Fig. 8(b,~~d,f), the coefficients change from a moderate positive relationship with no statistical significance (r=0.35, p=0.39) to a positive relationship with a marginal statistical significance (r=0.74, p=0.09). Despite the small sample size~~f). Although the sample size is small, particularly in cases with larger proportion of coarse particles (~~just~~six samples), the ~~strong correlation coefficient suggests a~~ progressively stronger correlation coefficients, combined with the well-established influence of variations in the imaginary part of the CRI on backscattering properties, suggests a potentially meaningful relationship between the hematite fraction and the lidar ratio, ~~at least so~~with a more marked tendency for the VIS portion of the spectrum at 532 nm.

This finding fits within the context from other studies that have looked for a relationship between the hematite fraction and absorption at different wavelengths. The study from Di Biagio et al. (2019) found a higher R^2 when analyzing the variation of the hematite fraction relative to the single scattering albedo at 520 nm (R^2=0.78) compared to 370 nm (R^2=0.73).

Overall, this analysis highlights that segregating dust plumes into size-based clusters, which reduce size variability within the analyzed dust plumes, leads to stronger correlation coefficients. This improvement is evident for the backscatter-related ÅE at the UV-VIS spectral range, as shown across all three cluster classifications in Fig. 8, regardless of the specific size classifications. However, this trend is not consistent for all the intensive optical properties, which reflects the complexity of the relationships. One possible explanation is that since different size categories impact dust optical properties in distinct ways. Specifically, absorption tends to dominate over scattering in coarser particles (Adebiyi and Kok, 2020; Di Biagio et al., 2019), which provides an explanation as to why the size cluster with the coarser particles, exhibits the strongest correlations for lidar ratios.

The impact of the particle size on the particle linear depolarization ratios, as noted by Hofer et al. (2020) and Miffre et al. (2023), δ increases with particle size and that is observable in Fig. 8. Specifically, the mean δ_{355} values rise from 0.21 in
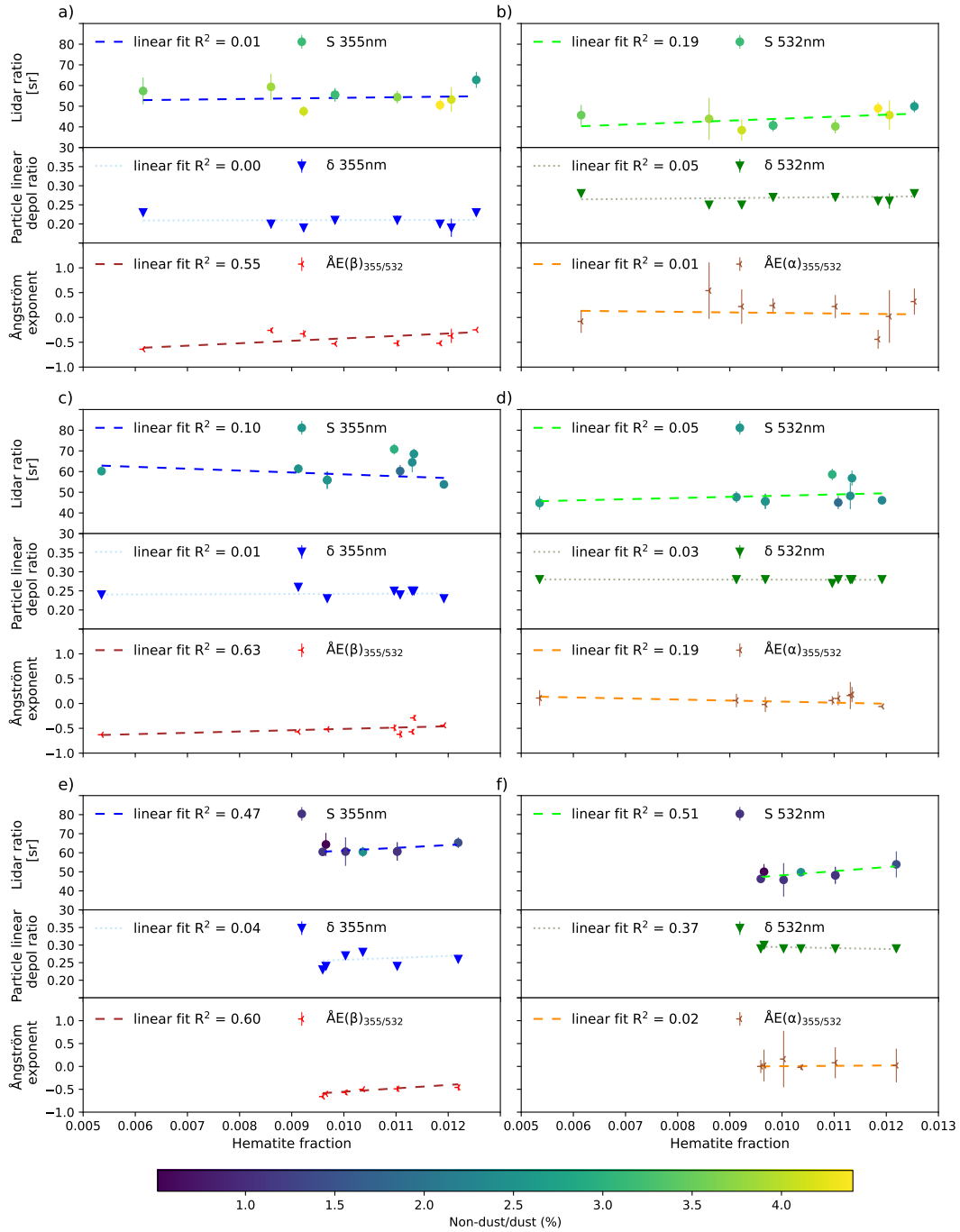
Figure 8. As in Fig. 7 but the color coding differs and the twenty two dust cases are separated regarding their fine-to-coarse fraction: (a-b) dust layers with fine/coarse above 0.11, (c-d) dust layers with fine/coarse above ~~0.9~~ 0.09 and below 0.11, and (e-f) dust layers with fine/coarse below ~~0.9~~ 0.09. (a,c,e) illustrate S_{355}, δ_{355}, and $\text{ÅE}(\beta)_{355/532}$, (b,d,f) shows the values related to S_{532}, δ_{532}, and $\text{ÅE}(\alpha)_{355/532}$. The color coding depend on the non-dust to dust fraction obtained from the POLIPHON method, values in percentage are shown by the color bar.

Table 3. Mean values and the ~~Person~~ linear correlation ~~coefficients (r~~coefficient, ~~p)~~ R^2, with respect to variations of the hematite fraction with lidar ratios (S), particle linear depolarization ratios (δ), backscatter-related Ångström exponent ($\mathring{A}E(\beta)$) and extinction-related Ångström exponent ($\mathring{A}E(\alpha)$) for the 355 nm and 532 nm wavelengths. Categorized according to size differences throughout the case studies following Fig. 3 based on the fine-to-coarse ratio (f/c) from the data obtained by appying the POLIPHON method.

fine(f)/coarse(c)	S_{355} [sr]	δ_{355}	S_{532} [sr]	δ_{532}	$\mathring{A}E(\beta)_{355/532}$
f/c > 11%	55±4	0.208±0.009	44±5	0.265±0.007	-0.43±0.06
(8 cases)	~~r~~R^2=~~-0.03, p=0.94~~0.01	~~r~~R^2=~~-0.22, p=0.59~~0	~~r~~R^2=~~0.35, p=0.39~~0.19	~~r~~R^2=~~-0.01, p=0.97~~0.05	~~r~~R^2=~~0.38, p=0.35~~0.5
9% < f/c < 11%	62±3	0.244±0.005	49±3	0.279±0.003	-0.52±0.04
(8 cases)	~~r~~R^2=~~0.16, p=0.71~~0.10	~~r~~R^2=~~-0.001, p=0.99~~0.01	~~r~~R^2=~~0.38, p=0.36~~0.05	~~r~~R^2=~~-0.16, p=0.7~~0.03	~~r~~R^2=~~0.52, p=0.18~~0.6
f/c < 9%	62±4	0.253±0.004	49±5	0.292±0.002	-0.55±0.04
(6 cases)	~~r~~R^2=~~0.46, p=0.36~~0.47	~~r~~R^2=~~0.26, p=0.62~~0.51	~~r~~R^2=~~0.74, p=0.09~~0.04	~~r~~R^2=~~-0.41, p=0.42~~0.37	~~r~~R^2=~~0.87, p=0.02~~0.6

Fig. 8(a), to 0.25 in Fig. 8(e) as shown in Table 3. A similarly increase in the mean δ_{532} values is observed. ~~However,~~ further validating the size clusters. Furthermore, the finding from Miffre et al. (2023) laboratory study ~~, which~~ showed that the presence of hematite lowers δ_{355}, is not reflected in these case studies. ~~A~~ However, a slight tendency pointing towards this relationship is shown in Fig. 8(f), where a weak negative correlation ~~(r=-0.41)~~ between δ_{532} and hematite fraction is observed ~~only~~ for the coarser particles case~~, Fig. 8(f), though this is paired with a high p-value (p=0.42). A moderate fit (R²=0.36) from the linear analysis is found between them (linear fit not shown).~~.

When examining the relationships between the backscatter-related Ångström exponent and hematite fractions, the ~~Pearson~~ linear correlation coefficients increase ~~as the portion of fine dust decreases~~the most between the cluster with finer particles and the intermediate and coarser classifications. In particular, the $\mathring{A}E(\beta)_{355/532}$ - hematite fraction analysis in ~~(f) shows a strong positive correlation with statistical significance (r=0.87 with p=0.02). The fitness of the linear relationship is correspondingly high (R²=0.6), portraying a moderately strong predictive ability.~~ Fig. 8(c) and (f) show strong positive correlations. Conversely, the $\mathring{A}E(\alpha)_{355/532}$ - hematite fraction analysis across varying particle sizes (b,d,e) shows ~~weakening negative correlations that lack statistical significance~~no correlation or consistent change within size clusters. Interestingly, the average values of $\mathring{A}E(\alpha)_{355/532}$ reduce towards zero as coarser particles become dominant, portraying the strength of the size dependency of this property.

Following Miffre et al. (2020) and Veselovskii et al. (2020), it is evident that the backscatter-related ~~Ångström exponent~~ ÅE for the 355 to 532 nm wavelengths is influenced by the ~~real and imaginary parts of the complex refractive index (CRI)~~imaginary part of the CRI. Even though the negative relationship found in Veselovskii et al. (2020)'s sensitivity study, where $\mathring{A}E(\beta)_{355/532}$ decreases as the imaginary part of the CRI increases, does not align with our findings, Miffre et al. (2020)'s laboratory study suggest a different scenario. In cases with larger effective radius and considering non-spherical particles, where the real part of the CRI does not vary, $\mathring{A}E(\beta)_{355/532}$ increases as the imaginary part of the CRI increases. Given that Di Biagio et al. (2019) observed no variation in the real part of the CRI of any dust samples at these wavelengths, it suggests that the changes in $\mathring{A}E(\beta)_{355/532}$ are primarily driven by variations in the imaginary part of the CRI, which in turn has been linked to hematite

content (Fig.9 in Di Biagio et al., 2019). This indicates that the observed changes shown here in the $\text{ÅE}(\beta)_{355/532}$ are a result of hematite's impact on the imaginary part of the CRI, which affects dust's backscattering capabilities differently for the 355 and 532 nm wavelengths. As shown in Fig.9 in Di Biagio et al., 2019, the relationships between hematite content and the imaginary part of the CRI and SSA exhibit steeper slopes at 355 nm compared to longer wavelengths, highlighting a wavelength dependency. If the increase in hematite content has a stronger effect on the backscattering coefficient at 355 nm than at 532 nm, this explains the observed rise in $\text{ÅE}(\beta)_{355/532}$ with increasing hematite content.

The lidar ratio-related ÅE analysis shows a similar results to $\text{ÅE}(\beta)_{355/532}$, showing the strongest correlation with the varying hematite fraction for the intermediate cluster (R^2=0.42). Furthermore, $\text{ÅE}(S)_{355/532}$ correlation coefficients get stronger between the cases with finer particles and the ones with coarser particles (see Fig. B2). These results reinforce the idea that hematite influences the lidar ratio with a wavelength dependence by impacting stronger S_{355} than S_{532}.

Additionally, the color coding provides further insight by highlighting the relationship between the non-dust to dust fraction, as derived from POLIPHON, within each dust layer. As shown in Fig. 8, the highest non-dust portions are found in the layers with the larger fine dust portion Fig. 8(a-b), and this ratio decreases progressively as the fine dust portion diminishes. The presence of higher non-dust content, such as soot - whether locally produced or transported within the layer - can influence the measured optical properties by absorbing radiation at UV wavelengths (Müller et al., 2009). This effect contributes into the understanding of the lack of clear, positive relationships between the S_{355}, S_{532}, $\text{ÅE}(\beta)_{355/532}$, and the increase of hematite content for cases a higher portion of non-dust aerosols.

We conclude that ~~due to~~ the complex interactions between ~~the~~ particle size, shape and composition with the intensive optical properties ~~,~~ make the effect of increased hematite fraction ~~on absorption becomes~~ more apparent only when dust cases are ~~separated, reducing size variations and minimizing~~ size segregated. This approach reduces size variations and minimizes interference from other aerosols. Although these separations are artificial due to the uncertainties of the fine-to-coarse ratios, they serve as a valuable exploratory analysis, highlighting the importance of size segregation in studying the impacts of iron oxide content on intensive optical properties.

4 Conclusion and implications

~~A positive relationship is found~~ Positive correlations are revealed in the analysis between lidar retrieved intensive optical properties and ~~modelled hematite fraction for~~ modeled hematite fraction in dust cases when ~~analysed separately according to particle size . These dust layers have a minor amount of fine dust fraction and minimal~~ considering particle size separately, especially for layers with minimal fine dust and non-dust content. ~~However, this does not mean that hematite has no impact on intensive optical properties in cases with more heterogeneous size distributions. Instead,~~ This suggests that both particle size and composition ~~both impact these properties of dust , though~~ significantly influence dust optical properties, although their effects are ~~difficult to separate. This complexity arises because~~ intertwined and difficult to disentangle due to their nonlinear nature. Furthermore, due to the nature of the POLIPHON method, ~~most~~ the concentration of non-dust particles ~~are concentrated~~

~~in the fine particle fraction~~ is contained within the fine fraction therefore obscuring the correlation between hematite and optical properties in this size range.

Regarding the positive correlation found with the backscatter-related Ångström exponent, our findings align with Miffre et al. (2020), indicating that an increase in the imaginary part of the CRI, linked to higher hematite content, leads to an increase in $\text{ÅE}(\beta)_{355/532}$. This supports the notion that changes in $\text{ÅE}(\beta)_{355/532}$ are primarily driven by variations in the imaginary ~~component~~ part of the CRI, rather than the real part. This is consistent with previous studies, such as those by Di Biagio et al. (2019), which found no variation in the real part of the CRI but identified hematite's impact on the imaginary part. ~~Although the~~ These correlations indicate a positive relationship between the hematite fraction and the dust's backscattering properties, with a wavelength-dependent influence. While the lidar ratio does not show a strong correlation ~~with changes in hematite content, there is~~ , a clear trend ~~where the positive correlation becomes stronger~~ emerges as particle size differences ~~decrease~~ become more constrained at both 355 nm and 532 nm wavelengths. ~~These correlations indicate a positive relationship between the hematite fraction and the dust's backscatter and extinction properties, with a wavelength-dependent influence.~~ In the size segregated cases, the positive correlation strengthens. This trend is further supported by the lidar ratio-related ÅE correlation analysis.

This study presents a framework for understanding the influence of hematite content on lidar measurements. To enhance the statistical validity of these findings, it is essential to identify additional lidar retrieved dust plumes that meet this study criteria, potentially using machine learning techniques. Expanding this research to other desert regions globally is also recommended, given the lidar ratio variations across different deserts (Hofer et al., 2020; Schuster et al., 2012).

Future modeling efforts should include a parametrization that takes into account the changes in particle size distribution as minerals get emitted, as well as adding the soil distribution content of goethite. Additionally, a new development could replace the use of soil interpolation produced databases by providing a mineralogical dataset from spaceborne hysperspectral measurements through NASA's Earth Surface Mineral Dust Source Investigation (EMIT: https://earth.jpl.nasa.gov/emit/).

Moreover, if a specific combination of lidar retrieved measurements can be identified for dust layers with varying hematite content, these measurements could be linked to distinct dust source regions with unique mineralogical distributions (Formenti et al., 2014; Go et al., 2022). This would build on previous studies that have linked differences in measured lidar ratios to dust originating from different regions of the Sahara Desert (Esselborn et al., 2009). To advance this research, efforts could also incorporate the infrared channel from Polly[XT] retrievals to identify minerals interacting with this part of the spectrum (Gebauer et al., 2024; Haarig et al., 2022).

To conclude, although a positive correlation has been identified between ~~lidar retrieved intensive optical properties~~ the backscatter-related Ångström exponent and hematite fraction, it is clear that further research is necessary in order to materialize and characterize this relationship and further relationships between hematite variations and lidar retrieved intensive optical properties. Nonetheless, these findings underscore the importance of considering both size and compositional factors for accurately representing dust optical properties. This could aid reduce uncertainties in model estimates of dust and its direct radiative effect.

Data availability. The dataset for reproducing the graphs presented here are available at http://doi.org/10.5281/zenodo.13908845.

640   Raw polly lidar observations (level 0 data, measured signals) can be accessed through the PollyNet database (http://polly.tropos.de/, last access on ~~October 2024~~February 2025).

Appendix A: Comparison between COSMO-MUSCAT-derived and AERONET AOT

A comparison of aerosol optical thickness (AOT) at 550 nm was conducted using AERONET data to evaluate the model's performance. The model derived AOT is calculated based on the simulated total column dust mass loads, an effective radius, a dimensionless dust extinction efficiency at 550 nm, which vary within the model size classifications, and a fixed, homogeneous density of 2650 kg/m^3. Further details of this diagnostic approach can be found in Gómez Maqueo Anaya et al. (2024). The comparison covered the entire simulation periods, from 8 August to 30 September 2021 and from 2 June to 31 July 2022. AERONET stations were strategically selected along the dust transport pathway from the Sahara Desert towards the Atlantic, and level 2.0 data, which undergo cloud screening, were used. The results are depicted in Fig. A1 for 2021 and Fig. A2 for 2022.

COSMO-MUSCAT performance varies across stations. While the model tends to underestimate AOT at certain stations, such as Mindeo and Banizoumbou during JATAC 2021, and Santa Cruz in both campaign periods, it generally overestimates AOT at the other studied stations. Among the stations analyzed, Santa Cruz station showed the best overall agreement with the modeled values. However, the lack of measurements at some stations during significant periods of time in both campaigns introduces bias into the model-observation correlations. Specific events, such as on 9 August 2021 at Cinzana and the midday of 23 August 2021 at Mindelo are significantly over represented and under represented by the model, respectively. The dust event recorded at the Banizoumbou station on the 13 September 2021 also appears to be under represented. However, satellite observations suggest potential cloud contamination in AERONET AOT values despite cloud screening procedures.

It is important to highlight that AERONET AOT retrievals account for all aerosol types potentially present, whereas the model simulates only dust aerosols. To ensure a more direct comparison, the focus is placed on periods when ÅE$(\alpha)_{440/870}$ values are below 0.3, which serves as a reliable indicator that dust is the dominant aerosol type (Ansmann et al., 2019). Despite these challenges, the model effectively reproduces the temporal evolution of dust plumes in the region, successfully captures the general patterns in timing and intensity. This suggest that the model provides a reliable representation of dust transport across the region and can be confidently used to simulate the life cycle of mineral dust aerosols.
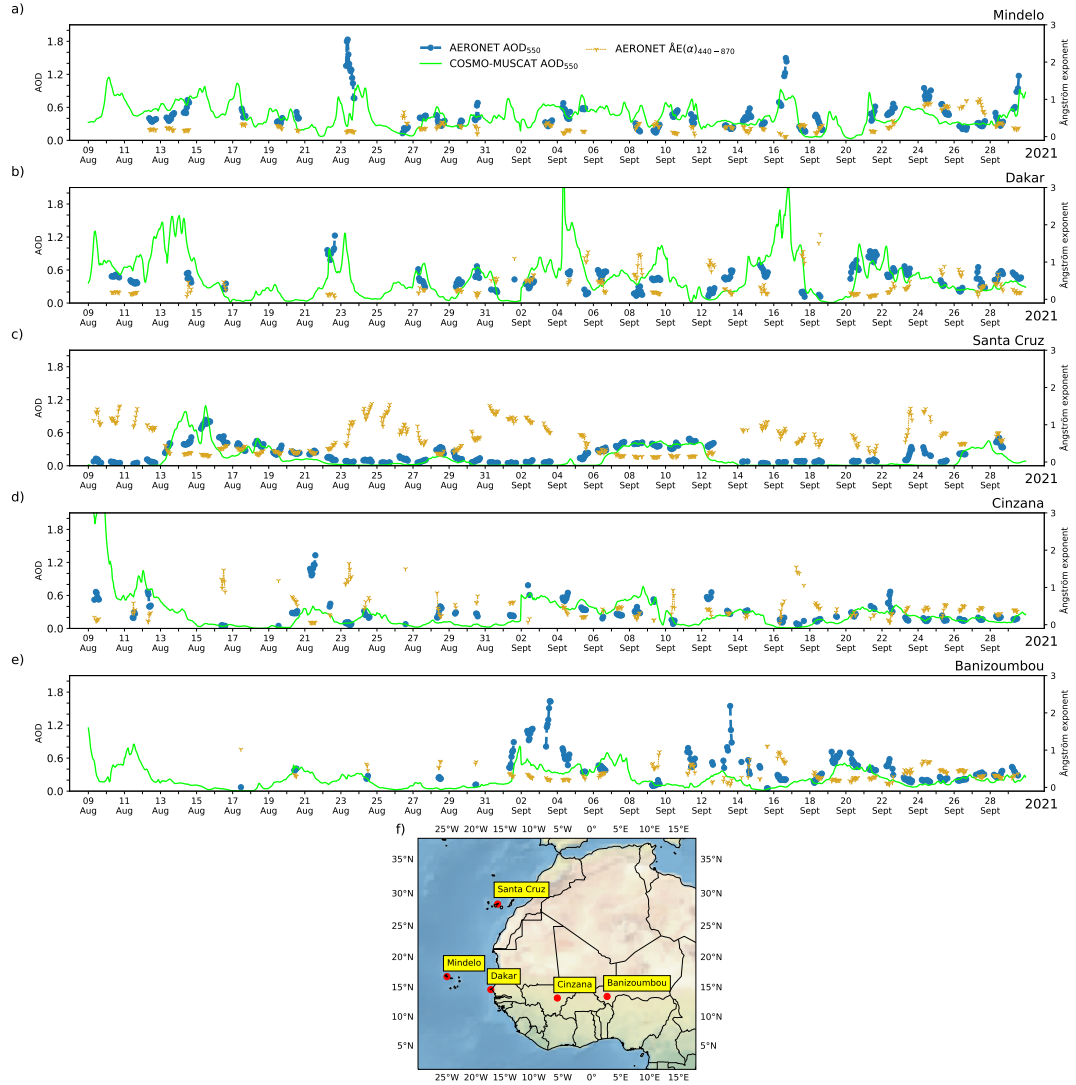
Figure A1. Dust AOT at 550 nm calculated from COSMO–MUSCAT dust concentration fields (green) and AOT at 550 nm and the exctintion-related Ångström exponent for the 440–870 nm wavelength range ($ÅE(\alpha)_{440/870}$) from AERONET, level 2.0, sun-photometer measurements (blue and gold), where each x-axis tick represents 12:00UTC for each day in the range of 8 August to 30 September 2021. Five different stations across the Sahara and downwind locations are shown. a) Mindelo (16.878°N, 24.995°W; Cape Verde), b) Dakar Belair (14.702°N, 17.426°W; Senegal), c) Santa Cruz Tenerife (28.473°N, 16.247°W; Spain), d) IER Cinzana (13.278°N, 5.934°W; Mali), e) Banizoumbou (13.547°N, 2.665°E; Niger), (f) AERONET station geographic locations and names used in this comparison.
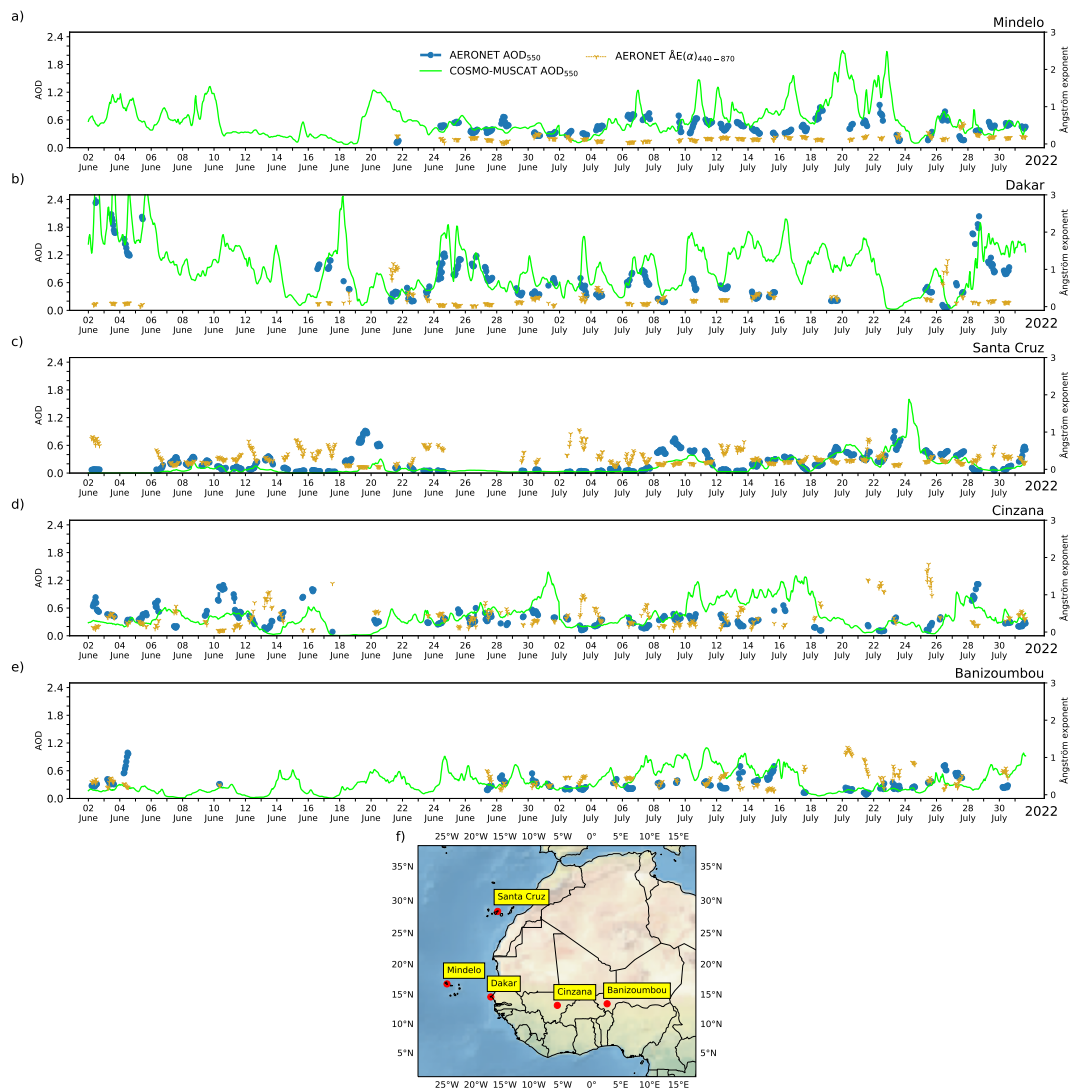
Figure A2. As in Fig. A1 but for the period of 2 June to 31 July 2022.
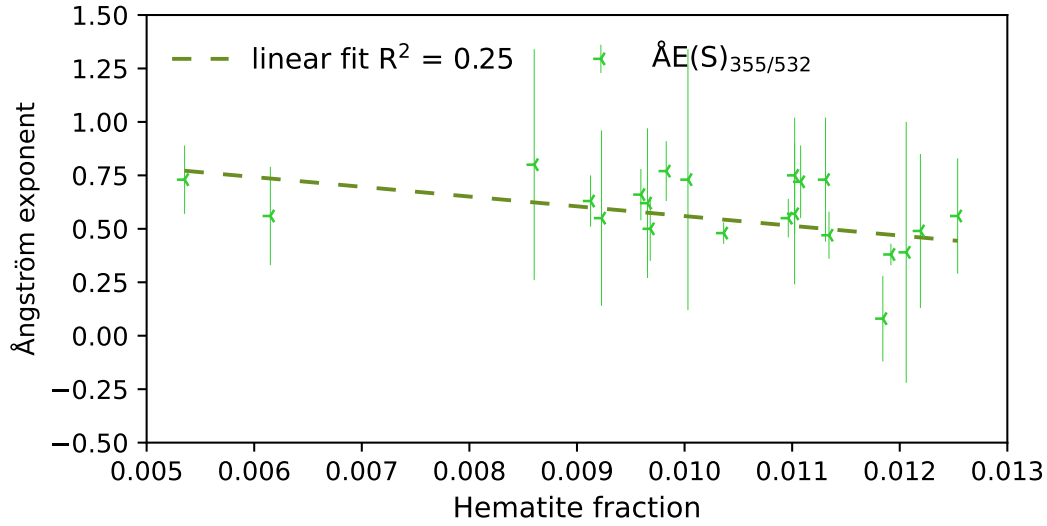
Figure B1. Mean values for 22 dust layers, hematite fractions are shown in the x axis and the lidar ratio-related Ångström exponent for the 355 and 532 nm is shown in the y axes. The standard deviation of $\mathrm{ÅE}(S)_{355/532}$ is shown by the error bar. Linear fit between the hematite fraction and $\mathrm{ÅE}(S)_{355/532}$ is illustrated by the dotted lines, the R squared value of the linear fit is shown in the dashed line legend.

665 **Appendix B: Lidar ratio Ångström exponent vs hematite fraction**

Figures B1 and B2 show the correlation analysis between averaged modeled hematite fraction and the lidar ratio-related Ångström exponent considering 22 dust layers. The lidar ratio-related Ångström exponent is derived from lidar measurements in the following way:

$$
\begin{aligned}
\mathrm{ÅE}(S)_{355/532} &= \frac{\ln(S_{355}/S_{532})}{\ln(355/532)} \\
&= \frac{\ln(\alpha_{355}/\beta_{355} * \beta_{532}/\alpha_{532})}{ln(355/532)} \\
&= \frac{\ln(\alpha_{355}/\alpha_{532}) + \ln(\beta_{532}/\beta_{355})}{ln(355/532)} \\
&= \mathrm{ÅE}(\alpha)_{355/532} - \mathrm{ÅE}(\beta)_{355/532}
\end{aligned}
\tag{B1}
$$
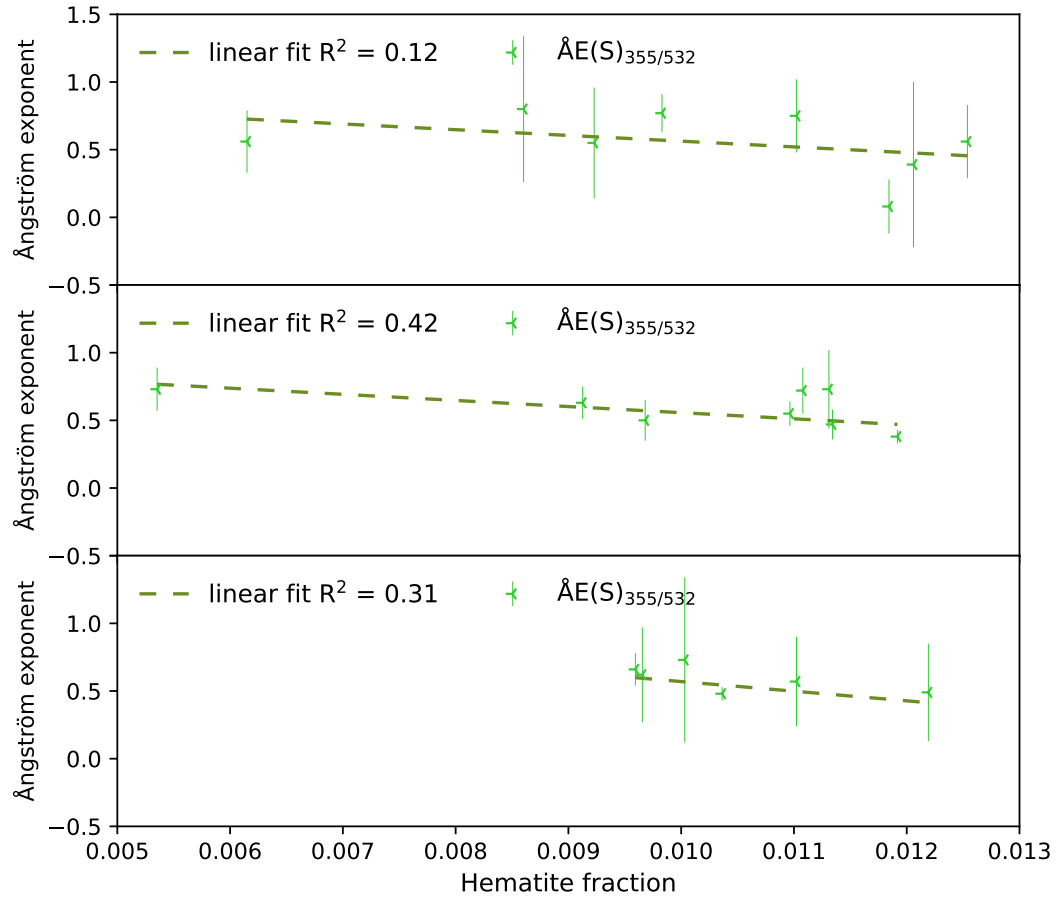
Figure B2. Same as Fig. B1 but for the case studies being separated regarding their fine-to-coarse fraction: first row shows dust layers with fine/coarse above 0.11, middle row illustrates dust layers with fine/coarse above 0.09 and below 0.11, and last row depicts dust layers with fine/coarse below 0.09.

Author contributions. SGMA wrote the manuscript draft; DA, KS, MH, JH, and BeHe reviewed and edited the manuscript; DA, KS, HB, and AA provided resources such as study materials, instrumentation, and analysis tools and were part of the conceptualization of the project; SGMA, DA, UW, MH, JH, HB, and AA were part of the formal analysis of lidar data. SGMA, KS, and DA performed the analysis of lidar data compared to ~~modelled~~ modeled results. MF – software development (restructured the code around MUSCAT dust emission scheme); SGMA, MF, BeHe, KS, and IT contributed to code development surrounding the mineralogy inclusion; AS, BiHe, HB, and RE are part of the maintenance and continuous improvement of the PollyXT lidar device(s).

Competing interests. The authors declare that they have no conflict of interest

Acknowledgements. This study is done in the framework of the DUSTRISK (a risk index for health effects of mineral dust and associated microbes) project, funded by the Leibniz Collaborative Excellence Programme Project (grant number K255/2019).

This research has been supported by the German Federal Ministry for Economic Affairs and Energy (BMWi) (grant no. 50EE1721C). Furthermore, we also acknowledge the support through ACTRIS-2 under grant agreement no. 654109 from the European Union's Horizon 2020 research and innovation programme and ACTRIS PPP under the Horizon 2020 – Research and Innovation Framework Programme, H2020-INFRADEV- 2016-2017, Grant Agreement number: 7395302.

We acknowledge and thank the team of OSCM / INMG for their crucial and ongoing support. We further thank ESA and the ASKOS/-JATAC teams for the organization of the JATAC(s) campaign(s) and their continuous support.

Further thanks are due to the Deutscher Wetterdienst (DWD) for cooperation and support, and to all PIs of the AERONET stations used in this study for maintaining the instruments, obtaining the measurements and providing data.

We want to thank all the TROPOS team involved in the PollyNET, the network dedicated to provide continuous aerosol data from automated Raman-polarizations lidars (Baars et al., 2016) https://polly.tropos.de/.

Muñoz Sabater, J., (2019, 2021) was downloaded from the Copernicus Climate Change Service (C3S) Climate Data Store. The results contain modified Copernicus Climate Change Service information 2020 and 2022. Neither the European Commission nor ECMWF is responsible for any use that may be made of the Copernicus information or data it contains.

Furthermore, ChatGPT was utilized to rephrase and shorten sentences, as well to identify the appropriate prepositions.

References

Adebiyi, A., Kok, J. F., Murray, B. J., Ryder, C. L., Stuut, J.-B. W., Kahn, R. A., Knippertz, P., Formenti, P., Mahowald, N. M., Pérez García-Pando, C., Klose, M., Ansmann, A., Samset, B. H., Ito, A., Balkanski, Y., Di Biagio, C., Romanias, M. N., Huang, Y., and Meng, J.: A review of coarse mineral dust in the Earth system, Aeolian Research, 60, 100 849, https://doi.org/10.1016/j.aeolia.2022.100849, 2023.

Adebiyi, A. A. and Kok, J. F.: Climate models miss most of the coarse dust in the atmosphere, Science Advances, 6, eaaz9507, https://doi.org/10.1126/sciadv.aaz9507, 2020.

Althausen, D., Engelmann, R., Baars, H., Heese, B., Ansmann, A., Müller, D., and Komppula, M.: Portable Raman Lidar PollyXT for Automated Profiling of Aerosol Backscatter, Extinction, and Depolarization, Journal of Atmospheric and Oceanic Technology, 26, 2366–2378, https://doi.org/10.1175/2009JTECHA1304.1, 2009.

Ångström, A.: On the Atmospheric Transmission of Sun Radiation and on Dust in the Air, Geografiska Annaler, 11, 156, https://doi.org/10.2307/519399, 1929.

Ansmann, A., Wandinger, U., Riebesell, M., Weitkamp, C., and Michaelis, W.: Independent measurement of extinction and backscatter profiles in cirrus clouds by using a combined Raman elastic-backscatter lidar, Applied Optics, 31, 7113–7131, https://doi.org/10.1364/AO.31.007113, 1992.

Ansmann, A., Seifert, P., Tesche, M., and Wandinger, U.: Profiling of fine and coarse particle mass: case studies of Saharan dust and Eyjafjallajökull/Grimsvötn volcanic plumes, Atmospheric Chemistry and Physics, 12, 9399–9415, https://doi.org/10.5194/acp-12-9399-2012, 2012.

Ansmann, A., Mamouri, R.-E., Hofer, J., Baars, H., Althausen, D., and Abdullaev, S. F.: Dust mass, cloud condensation nuclei, and ice-nucleating particle profiling with polarization lidar: updated POLIPHON conversion factors from global AERONET analysis, Atmospheric Measurement Techniques, 12, 4849–4865, https://doi.org/10.5194/amt-12-4849-2019, 2019.

Baars, H., Ansmann, A., Althausen, D., Engelmann, R., Heese, B., Müller, D., Artaxo, P., Paixao, M., Pauliquevis, T., and Souza, R.: Aerosol profiling with lidar in the Amazon Basin during the wet and dry season, Journal of Geophysical Research: Atmospheres, 117, 2012JD018 338, https://doi.org/10.1029/2012JD018338, 2012.

Baars, H., Kanitz, T., Engelmann, R., Althausen, D., Heese, B., Komppula, M., Preißler, J., Tesche, M., Ansmann, A., Wandinger, U., Lim, J.-H., Ahn, J. Y., Stachlewska, I. S., Amiridis, V., Marinou, E., Seifert, P., Hofer, J., Skupin, A., Schneider, F., Bohlmann, S., Foth, A., Bley, S., Pfüller, A., Giannakaki, E., Lihavainen, H., Viisanen, Y., Hooda, R. K., Pereira, S. N., Bortoli, D., Wagner, F., Mattis, I., Janicka, L., Markowicz, K. M., Achtert, P., Artaxo, P., Pauliquevis, T., Souza, R. A. F., Sharma, V. P., Van Zyl, P. G., Beukes, J. P., Sun, J., Rohwer, E. G., Deng, R., Mamouri, R.-E., and Zamorano, F.: An overview of the first decade of Polly^{NET}: an emerging network of automated Raman-polarization lidars for continuous aerosol profiling, Atmospheric Chemistry and Physics, 16, 5111–5137, https://doi.org/10.5194/acp-16-5111-2016, 2016.

Baars, H., Gebauer, H., Floutsi, A., Trapon, D., Bley, S., Althausen, D., Engelmann, R., Skupin, A., Radenz, M., Ansmann, A., Klamt, A., Heese, B., Wandinger, U., Silva, E., Rodrigues, E., Silva, P., Zenk, C., Paschou, P., and Marinou, E.: Quality assessment of Aeolus L2A products at Cabo Verde during JATAC and beyond - validation with ground-based lidar observations, in: EGU General Assembly 2023, p. 5631, EGU23, Vienna, Austria, https://doi.org/https://doi.org/10.5194/egusphere-egu23-5631, 2023.

Baldauf, M., Seifert, A., Förstner, J., Majewski, D., Raschendorfer, M., and Reinhardt, T.: Operational Convective-Scale Numerical Weather Prediction with the COSMO Model: Description and Sensitivities, Monthly Weather Review, 139, 3887–3905, https://doi.org/10.1175/MWR-D-10-05013.1, 2011.

730   Balkanski, Y., Schulz, M., Claquin, T., and Guibert, S.: Reevaluation of Mineral aerosol radiative forcings suggests a better agreement with satellite and AERONET data, Atmospheric Chemistry and Physics, 7, 81–95, https://doi.org/10.5194/acp-7-81-2007, 2007.

Berge, E.: Transboundary air pollution in Europe. Part 2: Numerical addendum to emissions, dispersion and trends of acidifying and eutrophying agents, Norske Meteorologiske Inst., Oslo (Norway), https://www.osti.gov/etdeweb/biblio/646220, 1997.

Boucher, O., Randall, D., Artaxo, P., Bretherton, C., Feingold, G., Forster, P., Kerminen, V.-M., Kondo, Y., Liao, H., Lohmann, U., Rasch,
735   P., Satheesh, S., Sherwood, S., Stevens, B., and Zhang, X.: Clouds and aerosols, in: Climate Change 2013: The Physical Science Basis. Contribution of Working Group I to the Fifth Assessment Report of the Intergovernmental Panel on Climate Change, edited by Stocker, T., Qin, D., Plattner, G.-K., Tignor, M., Allen, S., Doschung, J., Nauels, A., Xia, Y., Bex, V., Midgley, P., Fagerberg, J., Mowery, D. C., and Nelson, R. R., pp. 571–657, Cambridge University Press, https://doi.org/10.1017/CBO9781107415324.016, 2013.

Chatziparaschos, M., Daskalakis, N., Myriokefalitakis, S., Kalivitis, N., Nenes, A., Gonçalves Ageitos, M., Costa-Surós, M., Pérez García-
740   Pando, C., Zanoli, M., Vrekoussis, M., and Kanakidou, M.: Role of K-feldspar and quartz in global ice nucleation by mineral dust in mixed-phase clouds, Atmospheric Chemistry and Physics, 23, 1785–1801, https://doi.org/10.5194/acp-23-1785-2023, 2023.

Claquin, T., Schulz, M., and Balkanski, Y.: Modeling the mineralogy of atmospheric dust sources, Journal of Geophysical Research: Atmospheres, 104, 22 243–22 256, https://doi.org/10.1029/1999JD900416, 1999.

De Leeuw, G. and Lamberts, C.: Influence of refractive index and particle size interval on mie calculated backscatter and extinction, Journal
745   of Aerosol Science, 18, 131–138, https://doi.org/10.1016/0021-8502(87)90050-4, 1987.

Di Biagio, C., Formenti, P., Balkanski, Y., Caponi, L., Cazaunau, M., Pangui, E., Journet, E., Nowak, S., Caquineau, S., Andreae, M. O., Kandler, K., Saeed, T., Piketh, S., Seibert, D., Williams, E., and Doussin, J.-F.: Global scale variability of the mineral dust long-wave refractive index: a new dataset of in situ measurements for climate modeling and remote sensing, Atmospheric Chemistry and Physics, 17, 1901–1929, https://doi.org/10.5194/acp-17-1901-2017, 2017.

750   Di Biagio, C., Formenti, P., Balkanski, Y., Caponi, L., Cazaunau, M., Pangui, E., Journet, E., Nowak, S., Andreae, M. O., Kandler, K., Saeed, T., Piketh, S., Seibert, D., Williams, E., and Doussin, J.-F.: Complex refractive indices and single-scattering albedo of global dust aerosols in the shortwave spectrum and relationship to size and iron content, Atmospheric Chemistry and Physics, 19, 15 503–15 531, https://doi.org/10.5194/acp-19-15503-2019, 2019.

Di Biagio, C., Balkanski, Y., Albani, S., Boucher, O., and Formenti, P.: Direct Radiative Effect by Mineral Dust Aerosols Constrained by New
755   Microphysical and Spectral Optical Data, Geophysical Research Letters, 47, e2019GL086 186, https://doi.org/10.1029/2019GL086186, 2020.

Dubovik, O., Sinyuk, A., Lapyonok, T., Holben, B. N., Mishchenko, M., Yang, P., Eck, T. F., Volten, H., Muñoz, O., Veihelmann, B., Van Der Zande, W. J., Leon, J., Sorokin, M., and Slutsker, I.: Application of spheroid models to account for aerosol particle nonsphericity in remote sensing of desert dust, Journal of Geophysical Research: Atmospheres, 111, 2005JD006 619, https://doi.org/10.1029/2005JD006619,
760   2006.

Engelmann, R., Kanitz, T., Baars, H., Heese, B., Althausen, D., Skupin, A., Wandinger, U., Komppula, M., Stachlewska, I. S., Amiridis, V., Marinou, E., Mattis, I., Linné, H., and Ansmann, A.: The automated multiwavelength Raman polarization and water-vapor lidar Polly^\textrmXT: the neXT generation, Atmospheric Measurement Techniques, 9, 1767–1784, https://doi.org/10.5194/amt-9-1767-2016, 2016.

765   Esselborn, M., Wirth, M., Fix, A., Weinzierl, B., Rasp, K., Tesche, M., and Petzold, A.: Spatial distribution and optical properties of Saharan dust observed by airborne high spectral resolution lidar during SAMUM 2006, Tellus B: Chemical and Physical Meteorology, 61, 131, https://doi.org/10.1111/j.1600-0889.2008.00394.x, 2009.

Formenti, P., Schütz, L., Balkanski, Y., Desboeufs, K., Ebert, M., Kandler, K., Petzold, A., Scheuvens, D., Weinbruch, S., and Zhang, D.: Recent progress in understanding physical and chemical properties of African and Asian mineral dust, Atmospheric Chemistry and Physics, 11, 8231–8256, https://doi.org/10.5194/acp-11-8231-2011, 2011.

Formenti, P., Caquineau, S., Desboeufs, K., Klaver, A., Chevaillier, S., Journet, E., and Rajot, J. L.: Mapping the physico-chemical properties of mineral dust in western Africa: mineralogical composition, Atmospheric Chemistry and Physics, 14, 10 663–10 686, https://doi.org/10.5194/acp-14-10663-2014, 2014.

Freudenthaler, V., Esselborn, M., Wiegner, M., Heese, B., Tesche, M., Ansmann, A., Müller, D., Althausen, D., Wirth, M., Fix, A., Ehret, G., Knippertz, P., Toledano, C., Gasteiger, J., Garhammer, M., and Seefeldner, M.: Depolarization ratio profiling at several wavelengths in pure Saharan dust during SAMUM 2006, Tellus B: Chemical and Physical Meteorology, 61, 165, https://doi.org/10.1111/j.1600-0889.2008.00396.x, 2009.

Fuster, B., Sánchez-Zapero, J., Camacho, F., García-Santos, V., Verger, A., Lacaze, R., Weiss, M., Baret, F., and Smets, B.: Quality Assessment of PROBA-V LAI, fAPAR and fCOVER Collection 300 m Products of Copernicus Global Land Service, Remote Sensing, 12, 1017, https://doi.org/10.3390/rs12061017, 2020.

Gebauer, H., Floutsi, A. A., Haarig, M., Radenz, M., Engelmann, R., Althausen, D., Skupin, A., Ansmann, A., Zenk, C., and Baars, H.: Tropospheric sulfate from Cumbre Vieja (La Palma) observed over Cabo Verde contrasted with background conditions: a lidar case study of aerosol extinction, backscatter, depolarization and lidar ratio profiles at 355, 532 and 1064 nm, Atmospheric Chemistry and Physics, 24, 5047–5067, https://doi.org/10.5194/acp-24-5047-2024, 2024.

Go, S., Lyapustin, A., Schuster, G. L., Choi, M., Ginoux, P., Chin, M., Kalashnikova, O., Dubovik, O., Kim, J., Da Silva, A., Holben, B., and Reid, J. S.: Inferring iron-oxide species content in atmospheric mineral dust from DSCOVR EPIC observations, Atmospheric Chemistry and Physics, 22, 1395–1423, https://doi.org/10.5194/acp-22-1395-2022, 2022.

Gonçalves Ageitos, M., Obiso, V., Miller, R. L., Jorba, O., Klose, M., Dawson, M., Balkanski, Y., Perlwitz, J., Basart, S., Di Tomaso, E., Escribano, J., Macchia, F., Montané, G., Mahowald, N. M., Green, R. O., Thompson, D. R., and Pérez García-Pando, C.: Modeling dust mineralogical composition: sensitivity to soil mineralogy atlases and their expected climate impacts, Atmospheric Chemistry and Physics, 23, 8623–8657, https://doi.org/10.5194/acp-23-8623-2023, 2023.

Groß, S., Tesche, M., Freudenthaler, V., Toledano, C., Wiegner, M., Ansmann, A., Althausen, D., and Seefeldner, M.: Characterization of Saharan dust, marine aerosols and mixtures of biomass-burning aerosols and dust by means of multi-wavelength depolarization and Raman lidar measurements during SAMUM 2, Tellus B: Chemical and Physical Meteorology, 63, 706, https://doi.org/10.1111/j.1600-0889.2011.00556.x, 2011.

Groß, S., Freudenthaler, V., Schepanski, K., Toledano, C., Schäfler, A., Ansmann, A., and Weinzierl, B.: Optical properties of long-range transported Saharan dust over Barbados as measured by dual-wavelength depolarization Raman lidar measurements, Atmospheric Chemistry and Physics, 15, 11 067–11 080, https://doi.org/10.5194/acp-15-11067-2015, 2015.

Gómez Maqueo Anaya, S., Althausen, D., Faust, M., Baars, H., Heinold, B., Hofer, J., Tegen, I., Ansmann, A., Engelmann, R., Skupin, A., Heese, B., and Schepanski, K.: The implementation of dust mineralogy in COSMO5.05-MUSCAT, Geoscientific Model Development, 17, 1271–1295, https://doi.org/10.5194/gmd-17-1271-2024, 2024.

Haarig, M., Ansmann, A., Althausen, D., Klepel, A., Groß, S., Freudenthaler, V., Toledano, C., Mamouri, R.-E., Farrell, D. A., Prescod, D. A., Marinou, E., Burton, S. P., Gasteiger, J., Engelmann, R., and Baars, H.: Triple-wavelength depolarization-ratio profiling of Saharan dust over Barbados during SALTRACE in 2013 and 2014, Atmospheric Chemistry and Physics, 17, 10 767–10 794, https://doi.org/10.5194/acp-17-10767-2017, 2017.

Haarig, M., Walser, A., Ansmann, A., Dollner, M., Althausen, D., Sauer, D., Farrell, D., and Weinzierl, B.: Profiles of cloud condensation nuclei, dust mass concentration, and ice-nucleating-particle-relevant aerosol properties in the Saharan Air Layer over Barbados from polarization lidar and airborne in situ measurements, Atmospheric Chemistry and Physics, 19, 13 773–13 788, https://doi.org/10.5194/acp-19-13773-2019, 2019.

810 Haarig, M., Ansmann, A., Engelmann, R., Baars, H., Toledano, C., Torres, B., Althausen, D., Radenz, M., and Wandinger, U.: First triple-wavelength lidar observations of depolarization and extinction-to-backscatter ratios of Saharan dust, Atmospheric Chemistry and Physics, 22, 355–369, https://doi.org/10.5194/acp-22-355-2022, 2022.

Heinold, B., Tegen, I., Schepanski, K., Tesche, M., Esselborn, M., Freudenthaler, V., Gross, S., Kandler, K., Knippertz, P., Müller, D., Schladitz, A., Toledano, C., Weinzierl, B., Ansmann, A., Althausen, D., Müller, T., Petzold, A., and Wiedensohler, A.: Regional modelling

815 of Saharan dust and biomass-burning smoke: Part 1: Model description and evaluation, Tellus B: Chemical and Physical Meteorology, 63, 781–799, https://doi.org/10.1111/j.1600-0889.2011.00570.x, 2011.

Heinold, B., Tegen, I., Schepanski, K., and Banks, J. R.: New developments in the representation of Saharan dust sources in the aerosol–climate model ECHAM6-HAM2, Geoscientific Model Development, 9, 765–777, https://doi.org/10.5194/gmd-9-765-2016, 2016.

Highwood, E. J. and Ryder, C. L.: Radiative effects of dust, in: Mineral Dust: A Key Player in the Earth System, edited by: Knippertz, P. and

820 Stuut, Springer, https://doi.org/https://doi.org/10.1007/978-94-017-8978-3_13, 2014.

Hofer, J., Althausen, D., Abdullaev, S. F., Makhmudov, A. N., Nazarov, B. I., Schettler, G., Engelmann, R., Baars, H., Fomba, K. W., Müller, K., Heinold, B., Kandler, K., and Ansmann, A.: Long-term profiling of mineral dust and pollution aerosol with multiwavelength polarization Raman lidar at the Central Asian site of Dushanbe, Tajikistan: case studies, Atmospheric Chemistry and Physics, 17, 14 559–14 577, https://doi.org/10.5194/acp-17-14559-2017, 2017.

825 Hofer, J., Ansmann, A., Althausen, D., Engelmann, R., Baars, H., Fomba, K. W., Wandinger, U., Abdullaev, S. F., and Makhmudov, A. N.: Optical properties of Central Asian aerosol relevant for spaceborne lidar applications and aerosol typing at 355 and 532 nm, Atmospheric Chemistry and Physics, 20, 9265–9280, https://doi.org/10.5194/acp-20-9265-2020, 2020.

Holben, B. N., Eck, T. F., Slutsker, I., Tanré, D., Buis, J. P., Setzer, A., Vermote, E., Reagan, J. A., Kaufman, Y. J., Nakajima, T., Lavenu, F., Jankowiak, I., and Smirnov, A.: AERONET—A Federated Instrument Network and Data Archive for Aerosol Characterization, Remote

830 Sensing of Environment, 66, 1–16, https://doi.org/10.1016/S0034-4257(98)00031-5, 1998.

Huang, Y., Kok, J. F., Saito, M., and Muñoz, O.: Single-scattering properties of ellipsoidal dust aerosols constrained by measured dust shape distributions, Atmospheric Chemistry and Physics, 23, 2557–2577, https://doi.org/10.5194/acp-23-2557-2023, 2023.

Jakobsen, H. A., Berge, E., and Jonson, J. E.: The Multi-layer Eulerian Model: Model Description and Evaluation of Transboundary Fluxes of Sulphur and Nitrogen for One Year, DNMI Research Report 49, Meteorological Synthesizing Centre-West, https://books.google.de/

835 books?id=Lu8ivwEACAAJ, eCE Co-Operative Programme for and Europe, Evaluation of the Long Range Transmission of Air Pollutants in and Meteorological Synthesizing Centre–West (Oslo, Norway), 1997.

Journet, E., Balkanski, Y., and Harrison, S. P.: A new data set of soil mineralogy for dust-cycle modeling, Atmospheric Chemistry and Physics, 14, 3801–3816, https://doi.org/10.5194/acp-14-3801-2014, 2014.

Järvinen, E., Kemppinen, O., Nousiainen, T., Kociok, T., Möhler, O., Leisner, T., and Schnaiter, M.: Laboratory investigations of

840 mineral dust near-backscattering depolarization ratios, Journal of Quantitative Spectroscopy and Radiative Transfer, 178, 192–208, https://doi.org/10.1016/j.jqsrt.2016.02.003, 2016.

Kandler, K., Schütz, L., Deutscher, C., Ebert, M., Hofmann, H., Jäckel, S., Jaenicke, R., Knippertz, P., Lieke, K., Massling, A., Petzold, A., Schladitz, A., Weinzierl, B., Wiedensohler, A., Zorn, S., and Weinbruch, S.: Size distribution, mass concentration, chemical and

mineralogical composition and derived optical parameters of the boundary layer aerosol at Tinfou, Morocco, during SAMUM 2006, Tellus B: Chemical and Physical Meteorology, 61, 32, https://doi.org/10.1111/j.1600-0889.2008.00385.x, 2009.

Klett, J. D.: Lidar inversion with variable backscatter/extinction ratios, Applied Optics, 24, 1638, https://doi.org/10.1364/AO.24.001638, 1985.

Kok, J. F.: A scaling theory for the size distribution of emitted dust aerosols suggests climate models underestimate the size of the global dust cycle, Proceedings of the National Academy of Sciences, 108, 1016–1021, https://doi.org/10.1073/pnas.1014798108, 2011.

Kok, J. F., Ridley, D. A., Zhou, Q., Miller, R. L., Zhao, C., Heald, C. L., Ward, D. S., Albani, S., and Haustein, K.: Smaller desert dust cooling effect estimated from analysis of dust size and abundance, Nature Geoscience, 10, 274–278, https://doi.org/10.1038/ngeo2912, 2017.

Kok, J. F., Adebiyi, A. A., Albani, S., Balkanski, Y., Checa-Garcia, R., Chin, M., Colarco, P. R., Hamilton, D. S., Huang, Y., Ito, A., Klose, M., Li, L., Mahowald, N. M., Miller, R. L., Obiso, V., Pérez García-Pando, C., Rocha-Lima, A., and Wan, J. S.: Contribution of the world's main dust source regions to the global cycle of desert dust, Atmospheric Chemistry and Physics, 21, 8169–8193, https://doi.org/10.5194/acp-21-8169-2021, 2021.

Kok, J. F., Storelvmo, T., Karydis, V. A., Adebiyi, A. A., Mahowald, N. M., Evan, A. T., He, C., and Leung, D. M.: Mineral dust aerosol impacts on global climate and climate change, Nature Reviews Earth & Environment, 4, 71–86, https://doi.org/10.1038/s43017-022-00379-5, 2023.

Lafon, S., Rajot, J.-L., Alfaro, S. C., and Gaudichet, A.: Quantification of iron oxides in desert aerosol, Atmospheric Environment, 38, 1211–1218, https://doi.org/10.1016/j.atmosenv.2003.11.006, 2004.

Li, J., Carlson, B. E., Yung, Y. L., Lv, D., Hansen, J., Penner, J. E., Liao, H., Ramaswamy, V., Kahn, R. A., Zhang, P., Dubovik, O., Ding, A., Lacis, A. A., Zhang, L., and Dong, Y.: Scattering and absorbing aerosols in the climate system, Nature Reviews Earth & Environment, 3, 363–379, https://doi.org/10.1038/s43017-022-00296-7, 2022.

Li, L., Mahowald, N. M., Miller, R. L., Pérez García-Pando, C., Klose, M., Hamilton, D. S., Gonçalves Ageitos, M., Ginoux, P., Balkanski, Y., Green, R. O., Kalashnikova, O., Kok, J. F., Obiso, V., Paynter, D., and Thompson, D. R.: Quantifying the range of the dust direct radiative effect due to source mineralogy uncertainty, Atmospheric Chemistry and Physics, 21, 3973–4005, https://doi.org/10.5194/acp-21-3973-2021, 2021.

Li, L., Mahowald, N. M., Gonçalves Ageitos, M., Obiso, V., Miller, R. L., Pérez García-Pando, C., Di Biagio, C., Formenti, P., Brodrick, P. G., Clark, R. N., Green, R. O., Kokaly, R., Swayze, G., and Thompson, D. R.: Improved constraints on hematite refractive index for estimating climatic effects of dust aerosols, Communications Earth & Environment, 5, 295, https://doi.org/10.1038/s43247-024-01441-4, 2024.

Mahowald, N. M., Kloster, S., Engelstaedter, S., Moore, J. K., Mukhopadhyay, S., McConnell, J. R., Albani, S., Doney, S. C., Bhattacharya, A., Curran, M. a. J., Flanner, M. G., Hoffman, F. M., Lawrence, D. M., Lindsay, K., Mayewski, P. A., Neff, J., Rothenberg, D., Thomas, E., Thornton, P. E., and Zender, C. S.: Observed 20th century desert dust variability: impact on climate and biogeochemistry, Atmospheric Chemistry and Physics, 10, 10 875–10 893, https://doi.org/10.5194/acp-10-10875-2010, 2010.

Mamouri, R. E. and Ansmann, A.: Fine and coarse dust separation with polarization lidar, Atmospheric Measurement Techniques, 7, 3717–3735, https://doi.org/10.5194/amt-7-3717-2014, 2014.

Mamouri, R.-E. and Ansmann, A.: Potential of polarization/Raman lidar to separate fine dust, coarse dust, maritime, and anthropogenic aerosol profiles, Atmospheric Measurement Techniques, 10, 3403–3427, https://doi.org/10.5194/amt-10-3403-2017, 2017.

Marticorena, B. and Bergametti, G.: Modeling the atmospheric dust cycle: 1. Design of a soil-derived dust emission scheme, Journal of Geophysical Research: Atmospheres, 100, 16 415–16 430, https://doi.org/10.1029/95JD00690, 1995.

Menut, L., Siour, G., Bessagnet, B., Couvidat, F., Journet, E., Balkanski, Y., and Desboeufs, K.: Modelling the mineralogical composition and solubility of mineral dust in the Mediterranean area with CHIMERE 2017r4, Geoscientific Model Development, 13, 2051–2071, https://doi.org/10.5194/gmd-13-2051-2020, 2020.

885   Miffre, A., Cholleton, D., and Rairoux, P.: On the use of light polarization to investigate the size, shape, and refractive index dependence of backscattering Ångström exponents, Optics Letters, 45, 1084, https://doi.org/10.1364/OL.385107, 2020.

Miffre, A., Cholleton, D., Noël, C., and Rairoux, P.: Investigating the dependence of mineral dust depolarization on complex refractive index and size with a laboratory polarimeter at 180.0° lidar backscattering angle, Atmospheric Measurement Techniques, 16, 403–417, https://doi.org/10.5194/amt-16-403-2023, 2023.

890   Moosmüller, H., Engelbrecht, J. P., Skiba, M., Frey, G., Chakrabarty, R. K., and Arnott, W. P.: Single scattering albedo of fine mineral dust aerosols controlled by iron concentration, Journal of Geophysical Research: Atmospheres, 117, 2011JD016 909, https://doi.org/10.1029/2011JD016909, 2012.

Muñoz Sabater, J. and Copernicus Climate Change Service, S.: ERA5-Land hourly data from 2001 to present, https://doi.org/10.24381/CDS.E2161BAC, type: dataset, 2019.

895   Müller, D., Veselovskii, I., Kolgotin, A., Tesche, M., Ansmann, A., and Dubovik, O.: Vertical profiles of pure dust and mixed smoke–dust plumes inferred from inversion of multiwavelength Raman/polarization lidar data and comparison to AERONET retrievals and in situ observations, Applied Optics, 52, 3178, https://doi.org/10.1364/AO.52.003178, 2013.

Müller, T., Schladitz, A., Massling, A., Kaaden, N., Kandler, K., and Wiedensohler, A.: Spectral absorption coefficients and imaginary parts of refractive indices of Saharan dust during SAMUM-1, Tellus B: Chemical and Physical Meteorology, 61, 79, https://doi.org/10.1111/j.1600-
900   0889.2008.00399.x, 2009.

Nickovic, S., Vukovic, A., Vujadinovic, M., Djurdjevic, V., and Pejanovic, G.: Technical Note: High-resolution mineralogical database of dust-productive soils for atmospheric dust modeling, Atmospheric Chemistry and Physics, 12, 845–855, https://doi.org/10.5194/acp-12-845-2012, 2012.

Perlwitz, J. P., Pérez García-Pando, C., and Miller, R. L.: Predicting the mineral composition of dust aerosols – Part 1: Representing key
905   processes, Atmospheric Chemistry and Physics, 15, 11 593–11 627, https://doi.org/10.5194/acp-15-11593-2015, 2015a.

Perlwitz, J. P., Pérez García-Pando, C., and Miller, R. L.: Predicting the mineral composition of dust aerosols – Part 2: Model evaluation and identification of key processes with observations, Atmospheric Chemistry and Physics, 15, 11 629–11 652, https://doi.org/10.5194/acp-15-11629-2015, 2015b.

Poggio, L., de Sousa, L. M., Batjes, N. H., Heuvelink, G. B. M., Kempen, B., Ribeiro, E., and Rossiter, D.: SoilGrids 2.0: producing soil
910   information for the globe with quantified spatial uncertainty, SOIL, 7, 217–240, https://doi.org/10.5194/soil-7-217-2021, 2021.

Prigent, C., Aires, F., Rossow, W. B., and Robock, A.: Sensitivity of satellite microwave and infrared observations to soil moisture at a global scale: Relationship of satellite observations to in situ soil moisture measurements, Journal of Geophysical Research: Atmospheres, 110, https://doi.org/10.1029/2004JD005087, 2005.

Pérez García-Pando, C., Miller, R. L., Perlwitz, J. P., Rodríguez, S., and Prospero, J. M.: Predicting the mineral composition
915   of dust aerosols: Insights from elemental composition measured at the Izaña Observatory, Geophysical Research Letters, 43, https://doi.org/10.1002/2016GL069873, 2016.

Saito, M. and Yang, P.: Advanced Bulk Optical Models Linking the Backscattering and Microphysical Properties of Mineral Dust Aerosol, Geophysical Research Letters, 48, e2021GL095 121, https://doi.org/10.1029/2021GL095121, 2021.

Sakai, T., Nagai, T., Zaizen, Y., and Mano, Y.: Backscattering linear depolarization ratio measurements of mineral, sea-salt, and ammonium sulfate particles simulated in a laboratory chamber, Applied Optics, 49, 4441, https://doi.org/10.1364/AO.49.004441, 2010.

Scanza, R. A., Mahowald, N., Ghan, S., Zender, C. S., Kok, J. F., Liu, X., Zhang, Y., and Albani, S.: Modeling dust as component minerals in the Community Atmosphere Model: development of framework and impact on radiative forcing, Atmospheric Chemistry and Physics, 15, 537–561, https://doi.org/10.5194/acp-15-537-2015, 2015.

Schepanski, K., Tegen, I., Laurent, B., Heinold, B., and Macke, A.: A new Saharan dust source activation frequency map derived from MSG-SEVIRI IR-channels, Geophysical Research Letters, 34, https://doi.org/10.1029/2007GL030168, 2007.

Schepanski, K., Tegen, I., and Macke, A.: Saharan dust transport and deposition towards the tropical northern Atlantic, Atmospheric Chemistry and Physics, 9, 1173–1189, https://doi.org/10.5194/acp-9-1173-2009, 2009.

Schepanski, K., Mallet, M., Heinold, B., and Ulrich, M.: North African dust transport toward the western Mediterranean basin: atmospheric controls on dust source activation and transport pathways during June–July 2013, Atmospheric Chemistry and Physics, 16, 14 147–14 168, https://doi.org/10.5194/acp-16-14147-2016, 2016.

Schepanski, K., Heinold, B., and Tegen, I.: Harmattan, Saharan heat low, and West African monsoon circulation: modulations on the Saharan dust outflow towards the North Atlantic, Atmospheric Chemistry and Physics, 17, 10 223–10 243, https://doi.org/10.5194/acp-17-10223-2017, 2017.

Scheuvens, D., Schütz, L., Kandler, K., Ebert, M., and Weinbruch, S.: Bulk composition of northern African dust and its source sediments — A compilation, Earth-Science Reviews, 116, 170–194, https://doi.org/10.1016/j.earscirev.2012.08.005, 2013.

Schuster, G. L., Vaughan, M., MacDonnell, D., Su, W., Winker, D., Dubovik, O., Lapyonok, T., and Trepte, C.: Comparison of CALIPSO aerosol optical depth retrievals to AERONET measurements, and a climatology for the lidar ratio of dust, Atmospheric Chemistry and Physics, 12, 7431–7452, https://doi.org/10.5194/acp-12-7431-2012, 2012.

Seinfeld, J. H. and Pandis, S. N.: Atmospheric Chemistry and Physics: From Air Pollution to Climate Change, 3rd Edition \textbar Wiley, John Wiley & Sons, Hoboken, 3 edn., ISBN 978-1-118-94740-1, https://www.wiley.com/en-us/Atmospheric+Chemistry+and+Physics%3A+From+Air+Pollution+to+Climate+Change%2C+3rd+Edition-p-9781118947401, 2016.

Sokolik, I., Andronova, A., and Johnson, T. C.: Complex refractive index of atmospheric dust aerosols, Atmospheric Environment. Part A. General Topics, 27, 2495–2502, https://doi.org/10.1016/0960-1686(93)90021-P, 1993.

Sokolik, I. N. and Toon, O. B.: Direct radiative forcing by anthropogenic airborne mineral aerosols, Nature, 381, 681–683, https://doi.org/10.1038/381681a0, 1996.

Sokolik, I. N. and Toon, O. B.: Incorporation of mineralogical composition into models of the radiative properties of mineral aerosol from UV to IR wavelengths, Journal of Geophysical Research: Atmospheres, 104, 9423–9444, https://doi.org/10.1029/1998JD200048, 1999.

Solomos, S., Spyrou, C., Barreto, A., Rodríguez, S., González, Y., Neophytou, M. K. A., Mouzourides, P., Bartsotas, N. S., Kalogeri, C., Nickovic, S., Vukovic Vimic, A., Vujadinovic Mandic, M., Pejanovic, G., Cvetkovic, B., Amiridis, V., Sykioti, O., Gkikas, A., and Zerefos, C.: The Development of METAL-WRF Regional Model for the Description of Dust Mineralogy in the Atmosphere, Atmosphere, 14, 1615, https://doi.org/10.3390/atmos14111615, 2023.

Tegen, I., Harrison, S. P., Kohfeld, K., Prentice, I. C., Coe, M., and Heimann, M.: Impact of vegetation and preferential source areas on global dust aerosol: Results from a model study, Journal of Geophysical Research: Atmospheres, 107, AAC 14–1–AAC 14–27, https://doi.org/10.1029/2001JD000963, 2002.

Tegen, I., Schepanski, K., and Heinold, B.: Comparing two years of Saharan dust source activation obtained by regional modelling and satellite observations, Atmospheric Chemistry and Physics, 13, 2381–2390, https://doi.org/10.5194/acp-13-2381-2013, 2013.

Tesche, M., Ansmann, A., Müller, D., Althausen, D., Engelmann, R., Freudenthaler, V., and Groß, S.: Vertically resolved separation of dust and smoke over Cape Verde using multiwavelength Raman and polarization lidars during Saharan Mineral Dust Experiment 2008, Journal of Geophysical Research: Atmospheres, 114, 2009JD011 862, https://doi.org/10.1029/2009JD011862, 2009a.

960 Tesche, M., Ansmann, A., Müller, D., Althausen, D., Mattis, I., Heese, B., Freudenthaler, V., Wiegner, M., Esselborn, M., Pisani, G., and Knippertz, P.: Vertical profiling of Saharan dust with Raman lidars and airborne HSRL in southern Morocco during SAMUM, Tellus B: Chemical and Physical Meteorology, 61, 144, https://doi.org/10.1111/j.1600-0889.2008.00390.x, 2009b.

Tesche, M., Gross, S., Ansmann, A., Müller, D., Althausen, D., Freudenthaler, V., and Esselborn, M.: Profiling of Saharan dust and biomass-burning smoke with multiwavelength polarization Raman lidar at Cape Verde, Tellus B: Chemical and Physical Meteorology, 63, 649–676,

965 https://doi.org/10.1111/j.1600-0889.2011.00548.x, 2011.

Veselovskii, I., Goloub, P., Podvin, T., Bovchaliuk, V., Derimian, Y., Augustin, P., Fourmentin, M., Tanre, D., Korenskiy, M., Whiteman, D. N., Diallo, A., Ndiaye, T., Kolgotin, A., and Dubovik, O.: Retrieval of optical and physical properties of African dust from multi-wavelength Raman lidar measurements during the SHADOW campaign in Senegal, Atmospheric Chemistry and Physics, 16, 7013–7028, https://doi.org/10.5194/acp-16-7013-2016, 2016.

970 Veselovskii, I., Hu, Q., Goloub, P., Podvin, T., Korenskiy, M., Derimian, Y., Legrand, M., and Castellanos, P.: Variability in lidar-derived particle properties over West Africa due to changes in absorption: towards an understanding, Atmospheric Chemistry and Physics, 20, 6563–6581, https://doi.org/10.5194/acp-20-6563-2020, 2020.

Wagner, R., Ajtai, T., Kandler, K., Lieke, K., Linke, C., Müller, T., Schnaiter, M., and Vragel, M.: Complex refractive indices of Sa-haran dust samples at visible and near UV wavelengths: a laboratory study, Atmospheric Chemistry and Physics, 12, 2491–2512,

975 https://doi.org/10.5194/acp-12-2491-2012, 2012.

Wagner, R., Schepanski, K., Heinold, B., and Tegen, I.: Interannual variability in the Saharan dust source activation—Toward understanding the differences between 2007 and 2008, Journal of Geophysical Research: Atmospheres, 121, 4538–4562, https://doi.org/10.1002/2015JD024302, 2016.

Wandinger, U., Floutsi, A. A., Baars, H., Haarig, M., Ansmann, A., Hünerbein, A., Docter, N., Donovan, D., Van Zadelhoff, G.-J., Mason, S.,

980 and Cole, J.: HETEAC – the Hybrid End-To-End Aerosol Classification model for EarthCARE, Atmospheric Measurement Techniques, 16, 2485–2510, https://doi.org/10.5194/amt-16-2485-2023, 2023.

Weinzierl, B., Ansmann, A., Prospero, J. M., Althausen, D., Benker, N., Chouza, F., Dollner, M., Farrell, D., Fomba, W. K., Freudenthaler, V., Gasteiger, J., Groß, S., Haarig, M., Heinold, B., Kandler, K., Kristensen, T. B., Mayol-Bracero, O. L., Müller, T., Reitebuch, O., Sauer, D., Schäfler, A., Schepanski, K., Spanu, A., Tegen, I., Toledano, C., and Walser, A.: The Saharan Aerosol Long-Range Transport

985 and Aerosol–Cloud-Interaction Experiment: Overview and Selected Highlights, Bulletin of the American Meteorological Society, 98, 1427–1451, https://doi.org/10.1175/BAMS-D-15-00142.1, 2017.

Wolke, R. and Knoth, O.: Implicit–explicit Runge–Kutta methods applied to atmospheric chemistry-transport modelling, Environmental Modelling & Software, 15, 711–719, https://doi.org/10.1016/S1364-8152(00)00034-7, 2000.

Wolke, R., Schröder, W., Schrödner, R., and Renner, E.: Influence of grid resolution and meteorological forcing on simulated Eu-

990 ropean air quality: A sensitivity study with the modeling system COSMO–MUSCAT, Atmospheric Environment, 53, 110–130, https://doi.org/10.1016/j.atmosenv.2012.02.085, 2012.

Zhang, L., Gong, S., Padro, J., and Barrie, L.: A size-segregated particle dry deposition scheme for an atmospheric aerosol module, Atmo-spheric Environment, 35, 549–560, https://doi.org/10.1016/S1352-2310(00)00326-5, 2001.

Zhang, Y., Saito, M., Yang, P., Schuster, G., and Trepte, C.: Sensitivities of Spectral Optical Properties of Dust Aerosols to Their Mineralogical and Microphysical Properties, Journal of Geophysical Research: Atmospheres, 129, e2023JD040181, https://doi.org/10.1029/2023JD040181, 2024.